CHARACTERIZING THE HIGH PRESSURE BEHAVIOUR OF LUBRICANT BASESTOCKS

Clare McCabe[1], Peter T. Cummings[2,3], Scott Bair[4], Charles W. Manke[5]

[1]Department of Chemical Engineering, Colorado School of Mines, Golden CO 80401
[2]Departments of Chemical Engineering, Chemistry and Computer Science, University of Tennessee, Knoxville TN 37996
[3]Chemical Sciences Division, Oak Ridge National Laboratory, Oak Ridge TN
[4]George W. Woodruff School of Mechanical Engineering, Georgia Institute of Technology, Atlanta GA 30332
[5]Department of Chemical Engineering and Materials Science, Wayne State University, Detroit MI 48202

Introduction

Given the range of operating conditions lubricants are subjected to in practical applications (for example, in an automobile engine) a lubricant is often required to be effective over a wide range of temperature, speeds, and loads. Hence, a consideration of not only the viscosity, but also the viscosity-temperature and viscosity-pressure behaviour is needed to determine if a fluid would make a good lubricant component for a particular application. For example, it is essential that a lubricant retain a sufficiently high viscosity at normal operating temperatures (e.g., temperatures up to 100°C in the case of an automobile engine), whilst not being excessively high at the lowest temperatures (e.g., a cold start). The ideal lubricant would be one whose viscosity was minimally affected by the range of operating temperatures and pressures encountered. In reality, viscosity changes substantially with both temperature and pressure, though the extent of change depends on the chemistry and architecture of the lubricant molecules. Certain general trends in the structure–property relationships of hydrocarbon molecules are well known, for example while linear alkanes have very favourable viscosity-temperature behaviour they are solids at room temperature and so usually removed from the basestock during refining to improve the low temperature performance. By contrast, branched alkanes have a lower melting point, making them more suitable as lubricants, but have poorer viscosity-temperature behaviour. Hence obtaining the right balance is an important consideration.

Much of what is known about the physical properties of hydrocarbons is based on API Research Project 42 [1], a database of physical properties for pure hydrocarbons. Although API 42 contains some 273 entries, less than a quarter are in the C_{20}–C_{40} mass range, representing a minuscule fraction of the total number of possible structural isomers. Furthermore, very little experimental data is available in the literature on the high-pressure rheological properties of hydrocarbons, especially in the mass range of interest. The most comprehensive experimental study of the viscosity of lubricants to high pressures was undertaken at Harvard University [2] in the late 1940s, though more recently Bair and co-workers have measured the pressure-viscosity behaviour of liquid lubricants to pressures in the GPa range [3-4]. Hence, in order to provide a more complete datebase and obtain a clearer understanding of the influence of molecular architecture on viscous behaviour further experimentation is needed, though it is both costly and time consuming, especially at the severe conditions commonly found in engines and other machinery (e.g. film thickness < 1 micrometer, shear rates > 10^7 s^{-1}, pressure approximately = 10^9 Pa) which are extremely difficult to study experimentally.

Method

Over the last decade, with the exponential increase in computing power simulation techniques are proving to be an attractive and valuable means with which to "fill in the gaps" in the experimental data and obtain important structure-property information for lubricant basestocks. Using the non-equilibrium molecular dynamics (NEMD) technique, which is particularly suited to studying dynamic behaviour, there have been a number of simulation studies reported in the literature on the rheological properties of industrially important molecules [5]. For hydrocarbons, early work was limited to short, mainly linear molecules. However, with the recent advances in algorithms and the development of more realistic models it is now possible to perform simulations of more complex systems and more recently longer chains and branched molecules have been examined.

Results and Discussion

We present the results of non-equilibrium molecular dynamics simulations of alkanes in the C_{20}-C_{40} mass range, as this mass range form main constituents of lubricant basestocks, and hence their rheological properties are of great concern in industrial lubricant applications. The united atom model of Siepmann et al. [6] and Mondello and Grest [7], which has been shown to be successful in similar work, is used to describe the alkane molecules. From NEMD simulations at giga-pascal pressures and over a range of state conditions for each molecule studied we determine the strain rate dependant viscosity and the pressure-viscosity coefficient [8]. We show that the simulation results obey corresponding states behavior as seen in the rheology of polymer melts [9].

State Point	Temperature/K	Pressure/ GPa	Density/ gcm^{-3}
A	310.93	1.01E-04	0.791
B	372.04	1.01E-04	0.751
C	372.04	0.682	0.943
D	372.04	0.829	0.964
E	372.04	0.958	0.980

Table 1. State points studied for 9-octylheptadecane.

Through the generation of a "*master curve*", as illustrated in Figure 1 for 9-octylheptadecane at the state conditions given in Table 1, this

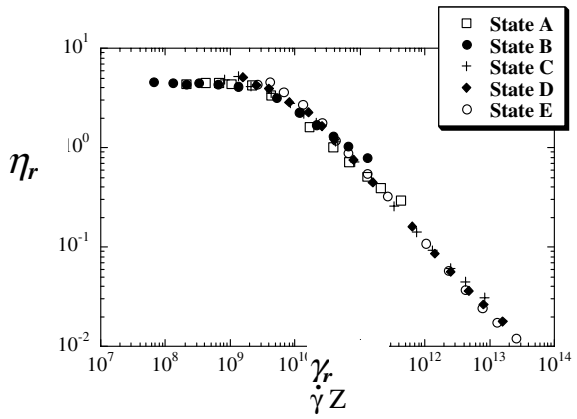

Figure 1. Reduced strain rate dependent viscosity for 9-octylheptadecane at state points given in Table 1. Taken from Reference 10.

yields the capability of quickly and efficiently predicting the Newtonian viscosity of lubricant components. Additionally, using low temperature shear-thinning viscosity measurements at GPa pressures, for the first time we demonstrate consistency between simulation and experiment in the Newtonian and non- Newtonian regimes [10].

Acknowledgement. This work was supported in part by the Division of Materials Sciences of the U. S. Department of Energy. The Oak Ridge National Laboratory is managed by UT-Battelle, LLC, for the Department of Energy under contract number DE-AC05-00OR22725. Additional funding was provided by Mobil Technology Company.

References

(1) *API 42: Properties of Hydrocarbons of High Molecular Weight*. American Petroleum Institute, New York, 1966.
(2) *ASME Research Committee on Lubrication, Pressure Viscosity Report*. Harvard University, New York, 1953.
(3) Bair, S. and Winer, W. O. (1992), 'The High Pressure High Shear Stress Rheology of Liquid Lubricants,' *Journal of Tribology*, **114**, 1-13.
(4) Bair, S. (2000), 'Pressure-Viscosity Behaviour of Lubricants to 1.4GPa and its Relation to EHD Traction,' *Tribology Transactions*, **43**, 91-99.
(5) Cummings, P. T. and Evans, D. J. (1992), 'Nonequilibrium Molecular Dynamics Approaches to Transport Properties and Non-Newtonian Fluid Rheology,' *I&EC Research*, **31**, 1237-1252.
(6) Smit, B., Karaborni, S. and I., S. J. (1995), 'Computer Simulations of the Vapor-Liquid Phase Equilibria of N-Alkanes,' *J. Chem. Phys.,* **102**, 2126.
(7) Mondello, M. and Grest, G. S. (1995), 'Molecular Dynamics of Linear and Branched Alkanes,' *J. Chem. Phys.*, **103**, 7156.
(8) McCabe, C., Cui, S. T., Cummings, P. T., Gordon, P. A. and Saeger, R. B. (2001), 'Examining the Rheology of 9-Octylheptadecane to Giga-Pascal Pressures,' *J. Chem. Phys.*, **114**, 1887-1891.
(9) S. Bair, C. McCabe, and P. T. Cummings, "Comparison of Non-Equilibrium Molecular Dynamics with Experimental Measurements in the Nonlinear Shear-Thinning Regime", *Physical Review Letters,* submitted for publication (2001).
(10) C. McCabe, C. W. Manke and P. T. Cummings, "Predicting the Newtonian Viscosity of Complex Fluids from High Strain Rate Molecular Simulations", *Journal of Chemical Physics,* accepted for publication.

CO chemisorption on flat and stepped Ni surfaces: A density functional study

Vaishali Shah[*], Tao Li[,#] Hansong Cheng[%], Kenneth Baumert[%], and David S. Sholl[*,#]*

[*]Department of Chemical Engineering, Carnegie Mellon University, Pittsburgh, PA 15213
[#]U. S. Department of Energy, National Energy Technology Laboratory, P. O. Box 10940, Pittsburgh PA 15236
[%]Air Products and Chemicals Inc., Allentown, PA 18195

Introduction

The adsorption of CO molecules on transition metal surfaces is one of the most widely studied problems in surface chemistry. CO is an important industrial gas. For example, mixtures of CO and H_2 (syngas) are used as precursors to liquid fuels and also to hydrogen fuels. Adsorption and desorption of CO on metal surfaces can lead to a range of desirable and undesirable chemical reactions. For example, contact between CO and Ni can corrode the solid phase nickel with the formation of gaseous nickel carbonyl. In the same system, adsorbed CO can dissociate to form carbonaceous surface species. This latter reaction is a serious problem in reforming applications where Ni is used as a catalyst. Many experimental and some theoretical studies have been performed to characterize and understand the CO interaction on Ni surfaces.[1,2] Despite this effort, there are a number of open problems and controversial issues concerning not only the preferred adsorption site, the structure of the CO layer at low and high coverages but also the nature of CO bond on these surfaces.[3-5] There is consensus however regarding the fact that steps and other surface defects are considerably more reactive than atomically flat surfaces.

In the present work we have examined the adsorption of CO on Ni(110) and Ni(210) surfaces using first principles density functional theory. Ni(110) is the least coordinated atomically flat Miller index surface and Ni(210) is characterized by a series of atomically straight step edges with (100) and (110) coordinations on either side of the step edge. CO adsorption at three sites, top, bridge and hollow is investigated. The purpose of this work is to gain insight into the preferred adsorption site for CO that can be then used in understanding the surface reactions available to CO on Ni surfaces.

Computational Method

Our density functional theory calculations are performed using the VASP (Vienna Ab initio simulation package) code[6-8] which is based on the Kohn-Sham density functional theory (DFT) formulation.[9] The electron-ion interactions are described by ultra soft pseudopotentials and exchange correlation energies are calculated with the generalized gradient approximation (GGA) as parameterized by Perdew and Wang.[10] A spin polarized computational scheme is employed since Ni is ferromagnetic. The bulk lattice constant of Ni was calculated to be 3.53 Å, in good agreement with experimental data.[11] The bond length of a gaseous CO molecule was calculated to be 1.15 Å, agreeing well with the calculations of Norskov *et. al.* [12]

The calculated bulk lattice constant was used to define the Ni(110) and Ni(210) surfaces. A (1x1) surface unit cell was chosen to minimize the number of atoms in the calculations and the surfaces were modeled by a slab consisting of five layers. The bottom two layers of the slab were held fixed allowing the top three layers to relax. CO was adsorbed on the topmost surface layer. We also performed these calculations with slabs consisting of three layers to check the minimum number of layers required for accurate results. In the three layer calculations the bottom layer was held fixed and the top two layers were allowed to relax. In the fully optimized five layer and three layer calculations good agreement is seen in the general trends observed in the interlayer separations as well as the percentage of contraction observed in the topmost layer. In each case, CO coverages corresponding to 1 molecule per surface atom were examined. The vacuum between the slabs when adsorbates are included is greater than 11 Å, large enough to ensure no significant interaction between the slabs.

The Brillouin zone of the surface unit cells was sampled with 5x5x1 Monkhorst-Pack mesh. An energy cutoff of 396.0 eV was used for the bare Ni surface as well as CO adsorbates on Ni surfaces. Full geometry optimizations were performed with the symmetry constraint using the conjugate gradient minimization scheme for systems consisting of less than 20 atoms and the quasi-Newton minimization scheme for systems consisting of more than 20 atoms. These two minimization methods were used solely for reasons of numerical efficiency. Calculations without the symmetry constraint for the atop and bridge sites on Ni(110) yielded equivalent results. The adsorption energy in each case is calculated according to the following equation $E_{ads} = E_{CO} + E_{Ni\ slab} - E_{CO/Ni\ slab}$, where E_{CO} is the total energy of an isolated CO molecule, $E_{Ni\ slab}$ is the total energy of the bare Ni(110) or Ni(210) surface and $E_{CO/Ni\ slab}$ is the total energy of the adsorbate on slab system. A positive E_{ads} corresponds to a stable adsorbate/slab system. The same Brillouin-zone sampling and energy cutoff were used in calculating the energies of the bare slab and adsorbate on slab system.

Results and Discussion

We have performed geometry optimizations for CO adsorbed at top, bridge and hollow site for Ni(110) and Ni(210) surfaces. These calculations were performed with both five layer surfaces and three layer surfaces. During these calculations all the atoms are allowed to relax completely except for the atoms in the fixed layers. In all the cases CO bonds to the surfaces via the C atom.

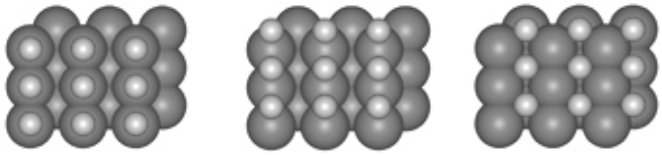

Figure 1. Adsorbate sites on Ni(110) surfaces. (a) top site, (b) bridge site and (c) hollow site.

The top view of the three adsorbate sites: top, short bridge (henceforth referred to as bridge) and four-fold hollow site for Ni(110) surface is shown in Figure 1. There is an additional adsorption site on Ni(110) surfaces, the long bridge site for which we have not reported any calculations in this work. The small light spheres correspond to the CO molecule and the large dark spheres correspond to the Ni(110) surface. Examining the energetics of the bare surface and the adsorbate on the Ni(110) surface, we observe that the net magnetic moment of the surface is slightly reduced in the presence of CO. The interlayer separations in the completely optimized five layer and three layer calculations agree with respect to the general trends observed as well as the percentage of contraction seen in the topmost layer.

Table 1 lists the adsorption energies at these three sites on Ni(110) and Ni(210) surfaces. The top site calculation was performed

with both five layer and three layer slabs. As can be seen, the agreement in the adsorption energy between these two calculations is very good. The distance between the Ni-C and C-O atoms also shows excellent agreement. Comparing the adsorption energies at the three sites, we observe that the bridge site is the most stable and the four-fold hollow site is the least stable. This trend in the adsorption energies and bond lengths of CO/Ni(110) is in agreement with that observed by Jenkins *et al*.[13] At the top and bridge site the C-O bond length is unchanged from its gas phase value but at the hollow site the C-O bond length has stretched by 1.8%. Our Ni-C and C-O bond lengths are again in good agreement with the spin polarized results of Jenkins *et al*.[13] Experimental investigation of CO adsorption on Ni(110) above atmospheric pressure[14] using x-ray diffraction measurements show that CO forms a (2x1) structure consisting of ordered zigzag arrangement of tilted molecules on short-bridge sites of the substrate with the Ni-C and C-O bond lengths to be 1.83 Å and 1.21 Å respectively. King *et. al.* have measured the calorimetric heat of adsorption of CO on single crystal Ni(110) surfaces at 0.12 monolayer (ML) to be 1.38 eV. [15]

Table 1. The adsorption energies, Ni-C and C-O bond lengths at the three sites for the 5 layer and 3 layer calculations on Ni(110) and Ni(210) surfaces.

	Site	# of layers	Eads (eV)	Ni-C Å	C-O Å
CO/Ni(110)	top	5	1.147	1.774	1.158
CO/Ni(110)	top	3	1.150	1.772	1.157
CO/Ni(110)	bridge	5	1.579	1.883	1.170
CO/Ni(110)	hollow	5	0.954	1.878	1.203
CO/Ni(210)	top	5	1.745	1.764	1.159
CO/Ni(210)	top	3	1.728	1.764	1.159
CO/Ni(210)	bridge	5	1.746	1.762	1.154
CO/Ni(210)	hollow	5	0.097	1.934	1.181

Our calculations on the Ni(210) surface with five layer and three layer slabs again agree with regard to the trends in the interlayer separations, the percentage contraction of the topmost layer, the adsorption energy and the distance between the Ni-C and C-O atoms, as seen from Table 1. As observed for CO/Ni(110), the presence of CO on Ni(210) slightly reduces the magnetic moment of the surface. The adsorption energies on the top and the bridge site are almost identical on Ni(210). The C-O bond length is once again unchanged from the gas phase value. The calculated adsorption energies show that the four fold hollow site is the least stable as also seen in the case of Ni(110) with the C-O bond length elongated by 3.4%.

Unlike Ni(110) there are no experimental or theoretical calculations performed to our knowledge on Ni(210) surfaces to compare our results with. There are however a wide variety of experiments performed on Ni(111) and Ni(100) surfaces. On Ni(100) experimental results show that CO is found in either the top or bridge site[4,16] for coverages < 0.5 ML LEED pattern studies and Extended Hückel Molecular Orbital calculations of CO at two fold and three-fold sites on Ni(111) surfaces[3] indicate that the three fold site is preferred at low coverages and as coverages increase the two-fold site and for higher coverages the top site is preferred for adsorption. On stepped Ni surfaces,[17,18] at low coverages CO is adsorbed in the step region and at increased coverages CO starts to adsorb on the terraces. CO adsorption on Pd(111) follows the same trend observed in Ni(111), however in Pt(111) at low coverages CO adsorbs at the top site and two fold bridge site and at high coverages CO is adsorbed exclusively at the top site similar to that seen in Ni(111) and Pd(111) surfaces.[3]

Conclusions and Ongoing Work

We have used DFT to study the adsorption of CO on flat Ni(110) and stepped Ni(210) surfaces. The adsorption energies are calculated from spin polarized plane wave calculations. Three adsorption sites were examined, namely the top, bridge and hollow sites. On both surfaces, the hollow site is found to be the least stable and the bridge site is found to be the most stable. The C-O and Ni-C bonds are elongated at the hollow site in comparison with the top site. Our calculations on five layer and three layer surfaces show good agreement in adsorption energies and bond lengths for both flat and stepped surfaces. Thus these surfaces can be successfully modeled using only three layers in the slabs.

We are currently extending these preliminary studies to look at several issues relevant to the chemical reactions available to CO on Ni surfaces. Specifically, we are examining the thermochemistry of Ni-carbonyl formation on atomically flat and stepped Ni surfaces. We are also applying DFT with the aim of quantitatively understanding the experimental observation that CO dissociates much more readily at surface steps and defects than on atomically flat planes.[19]

Acknowledgement. We gratefully acknowledge financial support from the Pennsylvania Infrastructure Technology Alliance and the National Energy Technology Laboratory and computing resources at the Pittsburgh Supercomputer Center.

References

(1) Dorsey, H. E.; Reutt-Robey, J. E. *Surf. Sci.,* **1997**, 380, 165.
(2) Brown, Robinson A.; Sinniah, K.; Reutt-Robey, J. E.; Doren, D. J.,*J. Chem. Phys*., **1994**, 101, 764.
(3) Wong, Y-T.; Hoffmann., R. *J. Phys. Chem*., **1991**, 95, 859.
(4) Föhlish, A.; Nyberg, M.; Bennich, P.; Triguero, L.; Hasselström, J.; Karis, O.; Petterson L. G. M.; Nilsson., A. *J. Chem. Phys*., **2000** 112, 1946.
(5) Hasselström, J.; Karis, O.; Petterson, L. G. M.; Föhlish, A.; Nyberg M.; Nilsson, A. *Phys. Rev. Lett*., **2000**, 85, 3309.
(6) Kresse, G.; Hafner, J. *Phys. Rev.*, **1993**, B 48, 13115.
(7) Kresse, G.; Furthmüller, J. *Comput. Mat. Sci*. **1996**, 6, 15.
(8) Kresse, G.; Furthmüller, *Phys. Rev*.. **1996**, B 54, 11169.
(9) Kohn, W.; Sham, L. J. *Phys. Rev*., **1965**, 140, A1133.
(10) Perdew, J. P.; Wang, Y. *Phys. Rev.*, **1992**, B 45, 13244.
(11) Kittel, C. *Introduction to Solid State Physic*s, John Wiley & Sons, 1976.
(12) Hammer, B.; Morikawa, Y.; Mortensen, J. J; Norskov, J. K. *Surf. Sci*., **1997**, 386, 66.
(13) Jenkins, S. J.; Ge, Q.; King, D. A. *Chem. Phys. Lett*., **2000**, 327, 125.
(14) Peters, K. F.; Walker, C. J.; Steadman, P.; Robach, O.; Isern, H.; Ferrer, S. *Phys. Rev. Lett*., **2001**, 86, 5325.
(15) Stuckless, J. T.; Al-Sararaf, N.; Wartnaby, C.; King, D. A. *J. Chem. Phys*., **1993**, 99, 2202.
(16) Pacchioni, G.; Chung, S-C.; Krüger, S.; Rösch, N. *Surf. Sci*., **1997**, 392, 173
(17) Sinniah, K.; Dorsett, H. E.; Reutt-Robey, J. E. *J. Chem. Phys*., **2000**, 112, 1958.
(18) Svensson, K.; Rickardsson, I.; Nyberg, C.; Andersoon, S. *Surf. Sci*., **1996**, 366, 140.
(19) Nakano, H.; Nakamura, J., *Surf. Sci*. **2001**, 482, 341.

Density Functional Theory Studies of Chemisorption and Diffusion Properties of Ni and Ni Complexes on MoS_2 Basal Planes

D. C. Sorescu , A. V. Cugini* and D. S. Sholl*,#*

*U. S. Department of Energy, National Energy Technology Laboratory, P. O. Box 10940, Pittsburgh, PA 15236.
#Dept. of Chemical Engineering, Carnegie Mellon University, Pittsburgh, PA. 15213

Introduction

Among various sulfide catalysts proposed for the hydrodesulfurization (HDS) process, molybdenum sulfide is one of most promising candidates for technological applications.[1,2] In practice it is used as well-dispersed MoS_2 nanocrystallites supported on γ-alumina and can be used both as an unpromoted or promoted catalyst[1] with Co or Ni atoms.

Despite a relative large number of experimental studies the role of the metallic promoters in HDS processes is still under intense debate. Recently, Weiss *et al.*[3-5] provided new insight based on low-temperature scanning tunneling microscopy investigations of the dynamics of Ni and Co clusters on MoS_2 basal planes. These studies indicate that both these species have a low barrier for surface diffusion. It was suggested that these promoters can be used to increase the sticking probability of sulfur-containing hydrocarbons and to transport these hydrocarbons to the active sites for reaction. However, several issues were not clarified by these studies. For example the location of the promoters on the basal plane or the electronic modifications induced upon adsorption of these metallic atoms is not well established. Moreover, the transport properties, particularly the diffusion characteristics as well as the clustering processes of these promoters on MoS_2 have not yet been well characterized and understood. Another issue raised by experimental investigations is that of the role played by various sulfur defects on the chemisorption properties of promoter atoms. In general, it would be very useful to understand how the adsorption and dissociation of various hydrocarbon species containing sulfur are changed in the presence of the promoters and of the vacancies on MoS_2 surface.

The properties of promoted MoS_2 catalysts have also been considered in several recent theoretical studies based on density functional theory (DFT) calculations.[6-7] However, these studies have focused exclusively on description of the binding properties of promoter species at edge surfaces where the catalytic activity is the highest but have not analyzed the properties of basal surfaces. In the present study we describe a DFT study that focuses on analyzing the interaction of Ni promoters with the basal plane of MoS_2 in an effort to clarify some of the mechanisms proposed by Weiss *et al.*[3-5] based on their STM investigations.

Computational Method

The calculations performed in this study were done using the Vienna *ab initio* simulation package (VASP).[8-10] This program evaluates the total energy of periodically repeating geometries based on density-functional theory and the pseudopotential approximation. In this case the electron-ion interaction is described by fully non-local optimized ultrasoft pseudopotentials similar to those introduced by Vanderbilt.[11,12] Periodic boundary conditions are used, with the one electron pseudo-orbitals expanded over a plane-wave basis set. The expansion includes all plane waves whose kinetic energy, $\hbar^2 k^2 / 2m < E_{cut}$ where k is the wave vector, m the electronic mass and E_{cut} is the chosen cutoff energy. A cutoff energy of 242 eV has been used in our studies.

Calculations have been done using the spin polarized PW91 generalized gradient approximation (GGA) of Perdew *et al.*[13] The sampling of the Brillouin zone was performed using a Monkhorst-Pack scheme.[14] The minimization of the electronic free energy was performed using an efficient iterative matrix-diagonalization routine based on a sequential band-by band residuum minimization method (RMM) or alternatively, based on preconditioned band-by-band conjugate-gradient (CG) minimization.[15] The optimization of different atomic configurations was performed based on a conjugate-gradient minimization of the total energy.

The minimum energy paths between different minima were optimized by use of the nudged elastic band (NEB) method of Jónsson and Mills.[16] In this approach the reaction path is "discretized", with the discrete configurations, or images, between minima being connected by elastic springs to prevent the images from sliding to the minima in the optimization. In the NEB searches either 8 or 16 images were employed between minima.

The periodic nature of the surface was represented in our simulations using a supercell model with periodic boundary conditions in all three directions. Most calculations have been done using a slab model consisting of one S-Mo-S layer. However, additional tests have been performed for the case of supercells with three S-Mo-S trilayers. In all calculations a vacuum layer of at least 10 Å has been used parallel to the MoS_2 basal plane

Results and Discussions

Based on full optimizations of the Ni atoms on the MoS_2 basal plane we have identified three stable adsorption configurations. The first one (1F) (see Fig.1a) corresponds to Ni atoms adsorbed on top of the sulfur atoms, the second one (6F) corresponds to a six-fold configuration of Ni (see Fig.1b).The last one (3F) is represented by adsorption on top of Mo atom with a three-fold binding to neighbor sulfur atoms (see Fig.1c).

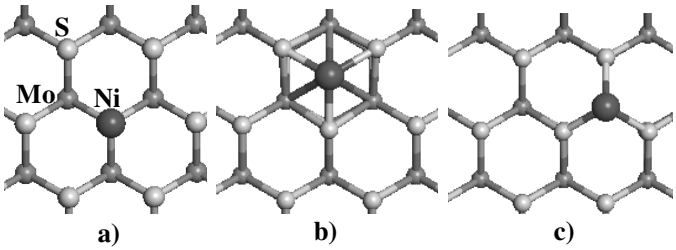

Figure 1. Adsorption configurations of Ni on MoS_2(0001) surface: (a) 1F on top of S atoms, (b) 6F in a six-fold configuration and (c) 3F on top of Mo atom.

Our results indicate a stability order E(3F) > E(6F) > E(1F). For the most stable adsorption configuration (3F), the adsorption energy, 77 kcal/mol, is large. In this configuration the Ni atom sits above the Mo atom at a distance of 2.59 Å while the Ni-S distances are 2.13 Å.

We have also investigated the minimum energy paths for diffusion of a Ni atom between different adsorption configurations using NEB calculations. In particular, we have analyzed three diffusion pathways suggested by the surface symmetry: 3F→6F→3F, 3F→6F→1F and 3F→1F. Our calculations indicate that among these the 3F→6F→3F pathway has the smallest barrier for diffusion. The corresponding profile determined in our studies is represented in Figure 2. As can be seen from this figure the barrier height is about 20 kcal/mol. This value is about 3.8 times smaller than the corresponding adsorption energy at the 3F site. This ratio of the

diffusion barrier to the adsorption energy is consistent with values obtained for other adsorbate/surface systems.[17] However, our results indicate much larger diffusion barriers than those expected from the analysis of STM data by Weiss et al.[3,4]

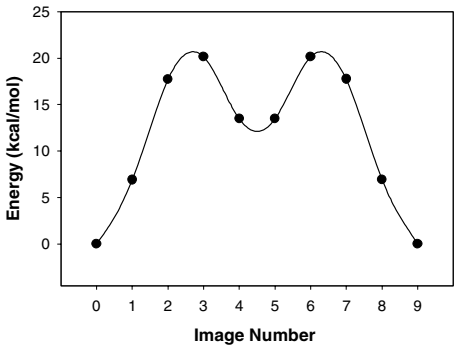

Figure 2. Minimum energy path for diffusion of Ni atom between two 3F sites and passing through the 6F configuration.

We have also analyzed the case when a Ni_3 cluster adsorbs on MoS_2 basal plane. We have identified an adsorption configuration on top of S atoms in which the adsorption energy per Ni atom decreases significantly to about 20.4 kcal/mol. However when this cluster is moved away from the on-top position the Ni atoms are adsorbed at the corresponding 3F sites, leading to cluster deformation and dissolution at the surface sites.

Another set of investigations we have pursued is related to adsorption of Ni atoms at S vacancy sites. Our calculations indicate that independent on the starting optimization configuration the Ni atom will adsorb at the position of S vacancy on the basal plane. The corresponding adsorption energy increases for this configuration to about 98.5 kcal/mol, indicating the existence of a very stable adsorption configuration.

As indicated by Weiss et al.[3-5] the presence of Ni atoms on MoS_2 surface is important to increase the sticking of sulfur-containing hydrocarbons. We have analyzed this aspect by performing studies of the adsorption of thiophene molecules on the promoted and unpromoted surfaces.

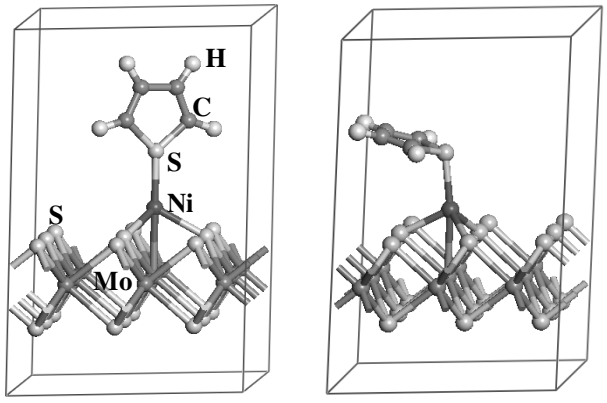

Figure 3. Vertical and tilted adsorption configurations of thiophene on Ni promoted MoS_2 basal plane.

In the case of adsorption of thiophene molecules on the unpromoted surface the calculated adsorption energies of thiophene are very small indicating a physisorption interaction mechanism. This result is in agreement with previous experimental findings determined by Salmeron et al.[18] based on TPD investigations. However, when Ni atoms are present on the surface the binding energies significantly increase. For example, in Figure 3 we present two possible adsorption configurations of thiophene molecule on Ni atoms positions at 3F sites. Our calculations indicate adsorption energies of about 20 kcal/mol for thiophene on the promoted surface. These results support the experimental findings related to the increased sticking probability of sulfur-containing hydrocarbons on basal surface.

Conclusions

The main results of our investigations related to adsorption and diffusion studies of Ni and Ni complexes on $MoS_2(0001)$ surface can be summarized as follows:

a) there are several adsorption configuration of Ni atoms on MoS_2 basal planes with large adsorption energies.

b) a simple hopping mechanism of Ni atoms between different adsorption sites indicate diffusion barriers in excess of 20 kcal/mol. This results contradict the experimental findings of Weiss et.al.[3,4] where metallic promoters were found to move easily on the surface even in the case of low temperatures.

c) the binding energy of Ni atoms to the surface increases when S vacancies are present.

d) the Ni promoter species increase the binding of thiophene molecule to the surface. In the absence of these promoters, thiophene physisorbs on the surface.

Acknowledgement. We gratefully acknowledge the supercomputer allocation provided by Pittsburgh Supercomputer Center under the SC^2 partnership program.

References

(1) Topsøe, H.; Clausen, B. S.; Franklin, F. E.; Massoth, E. in *Science and Technology in Catalysis: Hydrotreating Catalysis*; Anderson, J. R. Boudart, M., Ed.; vol. 11, Springer: Berlin, 1996.
(2) Kabe, T.; Ishihara, A.; Qqian, W. in *Hydrodesulfurization and Hydrogenation*, Wiley, New York, 1999.
(3) Kushmerick, J. G.; Weiss, P. S. *J. Phys. Chem.* B **1998**, 102, 10094.
(4) Kushmerick, J. G.; Han, K. P.; Johnson, J. A.; Weiss, P. S. *J. Phys. Chem.* B **2000**, 104, 2980.
(5) Kandell, S. A.; Weiss, P. S. *J. Phys. Chem.* B **2001**, 105, 8102.
(6) Byskov, L. S.; Nørskov, J. K.; Clausen, B. S.; Topsøe, H. *J. Catal*. **1999**, 187, 109.
(7) Raybaud, P.; Hafner, J.; Kresse, G.; Kasztelan, S.; Toulhoat, H. *J. Catal.* **2000**, 190, 128.
(8) Kresse, G.; Hafner, J. *Phys. Rev*. **1993**, B 48, 13115.
(9) Kresse, G. ; Furthmüller, J. *Comput. Mat. Sci*. **1996**, 6, 15.
(10) Kresse, G.; Furthmüller, J. *Phys. Rev.* **1996**, B 54, 11169.
(11) Vanderbilt, D. *Phys. Rev*. **1990**, B 41, 7892.
(12) Kresse, G; Hafner, J. *J. Phys. Condens. Matter* **1994**, 6, 8245.
(13) Perdew, J. P.; Chevary, J. A.; Vosko, S. H.; Jackson, K. A.; Pedersen, M. R.; Singh, D. J. and Frolhais, C. *Phys. Rev.* **1992**, B 46, 6671.
(14) Monkhorst, H. J.; Pack, J. D. *Phys. Rev*. **1976**, B 13, 5188.
(15) Kresse, G; Hafner, J. *Phys. Rev*. **1993**, B 47, 588.
(16) Mills, G.; Jónsson, H.; Schenter, G. K. *Surf. Sci.* **1995**, 324, 305.
(17) Gomer, R.; Rep. Prog. Phys. **1990**, 53, 917.
(18) Salmeron, M.; Somorjai, G.A.; Wold, A. Chianelli, R.; Liang K. S. Chem. Phys. Lett. **1982**, 90, 105.

DEVELOPMENT OF MODEL FUELS WITH VOLATILITIES THAT RESEMBLE THOSE OF REAL FUELS

Michael L. Greenfield

Chemistry and Environmental Science Department
Ford Motor Company
P.O. Box 2053, mail drop 3083/SRL
Dearborn, MI 48121

Introduction

Commercial fuels are typically hydrocarbon mixtures that contain tens to hundreds of components [1]. The many chemical compounds found in gasoline fuels range from light ends, such as propane and butane, to heavy ends that boil at temperatures above 450 K. The wide range of compounds in fuel lead to it boiling and evaporating over a range of temperatures.

Vehicle performance depends in part on the fuel used. For example, the range of vaporization temperatures has been correlated with an empirical "drivability" parameter, which roughly describes how well a vehicle drives when using a particular fuel. It is thus desirable for engine and vehicle models to have clear mechanisms for incorporating differences among many different fuels. However, incorporating complete chemical detail into large-scale engine models becomes intractable for a fuel that contains hundreds of species. Fuels with only 5–10 components must be used instead.

Fuel volatility is typically measured using the ASTM D86 procedure [2]. In this test, 100 mL of fuel are heated. Fuel vapors are collected via a condenser, and enough heat is applied such that 4 mL of fuel condensate is collected each minute. The result of the measurement is data for the fuel vapor temperature as a function of the percent of fuel evaporated. The shape of the resulting plot—the so-called "D86 curve"—is a characteristic of any particular fuel. In practice, the composition of a commercial fuel varies to some extent from batch to batch, leading to slight changes in the D86 curve. In this sense, the D86 curve is not a true physical property; instead it is a mixture property tunable to meet prescribed specifications.

In previous work, we developed a computer model that predicts the D86 curve for a fuel, given the identity of each fuel component and its concentration [3]. In this work, we have used that model to develop model hydrocarbon mixtures whose compositions, vapor pressures, and distillation properties resemble those of two real fuels. These mixtures are both simple enough to use in analytical engine models and complicated enough to use in interpreting measurements of fuel volatility, fuel evaporation, and fuel permeation. Their research octane numbers also allow them to be used in an engine.

Modeling Approach

Two fuels were modeled in this study. Certification fuel (sometimes called indolene, a trademark of BP) is used in vehicle emissions certification tests, making this fuel important to include in engine models. The second fuel is an oxygenated fuel, included to illustrate the level of physicochemical nonideality that can arise.

The compounds to use in the model fuels were chosen using a variety of criteria. Beginning with a speciation of certification fuel, eight compounds were selected to span the range of boiling points found in the real fuel. Their molecular architecture (straight vs branched vs cyclic, alkane vs aromatic) and molecular weight were chosen to span the range found in a PIANO (paraffin, isoparaffin, aromatic, naphthenic, olefin) analysis of the same fuel. Ethanol was added to the component list for the oxygenated fuel.

The model requires several parameters for each component in the fuel, such as critical properties, solubility parameter, ideal gas heat capacity, and vapor pressure. We used correlations to estimate other required properties. Instrument-related model parameters were determined by matching the predicted D86 curve to experimental results for a 7-component synthetic fuel available at Ford. All the molecular and instrument parameters are described in detail in our previous work [3]. We modeled the fugacity of each component in each phase using either an ideal or nonideal approach. An ideal solution and vapor approach has the advantage that each component's volatility depends only on its concentration and pure-component properties; its volatility is independent of the identity and relative concentrations of all other compounds. Nonideal behavior was represented using vapor-phase fugacity coefficients, calculated via critical-property-based correlations [4], and liquid-phase activity coefficients, calculated using the group-contribution-based UNIFAC model [5,6]. The nonideal phase behavior approach is more realistic from a chemical viewpoint but leads to the volatility of each component being a function of temperature and of the concentration of all species in the same phase. For a fuel of known composition, predictions using a fully nonideal approach would be most likely to agree with experimental results.

Results and Discussion

The ultimate results from running our calculations are compositions of model fuels with volatilities representative of those of real fuel mixtures. These compositions depend on the fuel of interest, since different fuels have different volatilities, and on whether an ideal or nonideal approach is used for the phase equilibrium. Table 1 contains recommended compositions for use in ideal solution-based models. Each model fuel is made up of 7 or 8 compounds. These compositions, as shown in the figures below, are predicted to vaporize within an ideal model in very similar ways to how real fuel vaporizes in a real experiment. However, if the volatility of a mixture with a listed fuel composition was measured in a lab, the measured D86 curve is not expected to agree with the experimental D86 curve for the corresponding fuel. This disagreement would occur because no mixture of fuel components would behave exactly like an ideal solution in equilibrium with an ideal gas mixture.

Table 1. Amounts of Each Component in Model Fuels for Use in Ideal Liquid and Vapor Models.

Fuel	nC_4	iC_5	EtOH	nC_6	iC_8	nC_8	tol[a]	124-TMB[b]	nC_{13}
Certification	4	16		2.5	32		25.5	18	2
Oxygenated	6	34	5	10		11	20	12	2

Compound descriptions: (a) toluene, (b) 1,2,4-trimethylbenzene

Table 2 contains model fuel compositions recommended for use in nonideal solution models or in experimental applications in which a simplified fuel of fewer than 10 compounds is required. We expect that the fuel volatility of these mixtures, if mixed in the lab and measured experimentally, would show reasonably good agreement with the experimental D86 curve for their corresponding fuels. The predicted D86 curves are in excellent agreement with the experimental curves for the corresponding fuels, as shown below.

The experimental D86 curve and predictions from the ideal and nonideal models for certification fuel are shown in Figure 1. Experimental results are indicated by squares and circles. Throughout the measurement, the vaporization temperature increases with respect to the volume fraction distilled. Below 40 volume % distilled, there is slight disagreement of order 6°C between the two data sets. At 80 vol%, the vapor temperature begins to increase at a faster rate relative to the vaporization, causing a kink in the D86 curve. Our model predictions, calculated using a nonideal or ideal model, are shown by the dashed and solid lines, respectively. At low

vol%, the model results pass between the two data sets. At higher vol%, they are in good agreement with both sets and follow the kink at 80 vol%. The model fuel compositions from both approaches are close to one another, indicating near-ideal behavior.

Lines with filled points indicate mass fractions for model fuel components remaining in the liquid phase, using the nonideal model. These compositions provide an estimate of the composition that remains after partial evaporation (useful from the perspective of fuel handling). At low to moderate vol% distilled, the concentrations of n-butane, isopentane, and n-hexane decrease. Their disappearance is followed by increases and then decreases in isooctane, toluene, and 1,2,4-trimethylbenzene concentrations. The peaks indicate that isooctane, for example, is a larger fraction of the continuously decreasing amount of liquid in the flask. The kink in the D86 curve is predicted to occur when the toluene concentration approaches zero. In this model fuel, the kink occurs because there is a 60°C difference in boiling point between toluene and 1,2,4-trimethylbenzene. For real certification fuel, this suggests that few compounds are present with boiling temperatures between 111 and 170°C.

Table 2. Amounts of Each Component in Model Fuels for Use in Nonideal Liquid and Vapor Models or in Experiments Using Fuel Mixtures that Mimic Real Fuels.

Fuel	nC_4	iC_5	EtOH	C_6	iC_8	nC_8	Tol	124-TMB	nC_{13}
Certification	5	13		3[a]	31		27	19	2
Oxygenated	5.25	23.75	13	10[b]		10	24	12	2

a) n-hexane, b) cyclohexane

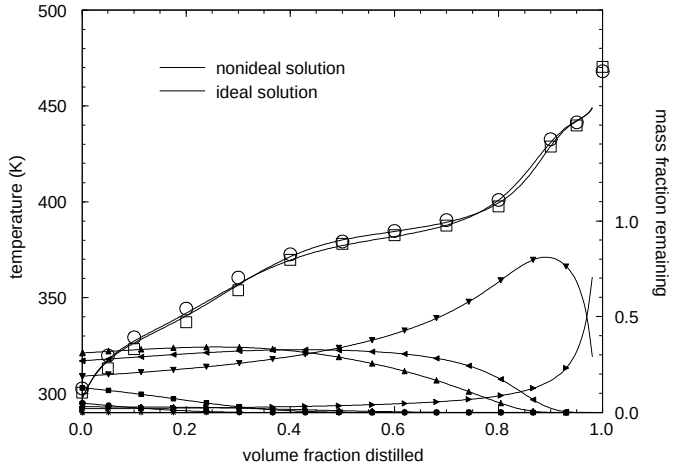

Figure 1. Distillation curve for real certification fuel and predictions using the D86 fuel distillation model. Model fuel compositions are based on ideal (straight line) and nonideal (dashed line) phase behavior. Dashed lines below the D86 data indicate the mass fractions of nC_4 (circles), iC_5 (squares), nC_6 (diamonds), iC_8 (up triangles), toluene (left triangles), 124-trimethylbenzene (down triangles), and nC_{13} (right triangles) in the undistilled fuel.

Figure 2 indicates the corresponding results for the oxygenated fuel. We find qualitatively similar results for this fuel. Here the kink (at 60 vol%) is due to the disappearance of ethanol, which is very nonideal (activity coefficient near 4). The nonideal solution model can capture this kink well. Our ideal solution model is tuned to follow the approximate curvature, but it deviates from the real fuel in two ways. First, no kink is present, because the fuel compounds are too close to one another in boiling point. Second, the required concentrations are significantly different from those in the real fuel. This is especially seen for ethanol: only 5% is optimal for the ideal model, compared to 13% in the nonideal model (and in the real fuel).

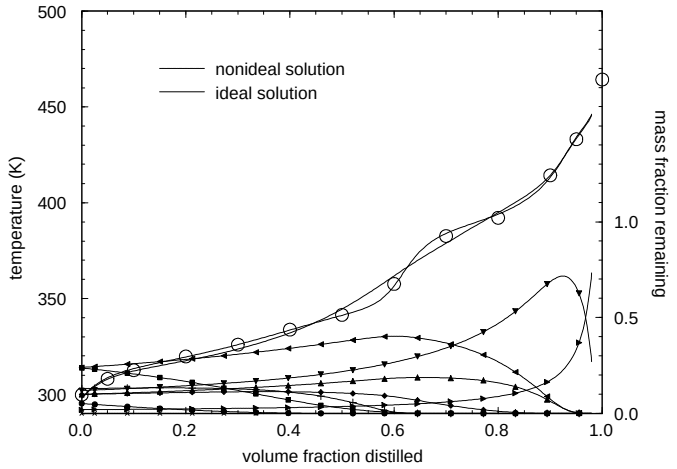

Figure 2. Distillation curve for oxygenated fuel and predictions using the D86 fuel distillation model. Model fuel compositions are based on ideal and nonideal phase behavior. Dashed lines below the D86 data indicate the mass fractions. Labels are the same as in Figure 1, with ethanol indicated by a plus (+).

The compounds used in this work do not represent the full spectrum of compounds found in a real fuel. For some compounds (typically n-butane and isopentane), the concentration in a model fuel is near the amount found in real fuel. This is because there are few compounds of comparable size and boiling point. For other compounds (isooctane, 1,2,4-trimethylbenzene, decane, tridecane), there is a significantly larger mass fraction in the model fuel than in a real fuel. This is because a single compound in the model fuel vaporizes in place of several compounds with similar structures and boiling points. For example, isooctane (2,2,4-trimethylpentane) represents other trimethylpentanes, assorted dimethylhexanes, and methylheptanes. It also represents compounds of similar molecular weight, such as dimethylpentanes and trimethylhexanes.

Conclusions

A macroscopic model of the D86 fuel distillation process can be used to create model fuels that display volatilities that equal those of real fuels used in vehicle testing and operation. Using less than 10 components in the mixture, it is possible to reproduce the entire distillation curve. Results are presented here for two fuels: a certification fuel and an oxygenated fuel. For the certification fuel, similar model fuel compositions result from using nonideal or ideal thermodynamics. For the oxygenated fuel, these approaches lead to qualitatively different fuel compositions and distillation curves. The resulting compositions can be used in engine models or in studies of fuel volatility, evaporation, or permeation.

Acknowledgement. We thank George Lavoie, Eric Curtis, Pete Misangyi, and Mira Burbaroska of Ford Motor Company for assistance with the properties of the real fuels.

References

(1) Owen, K.; Coley, T. *Automotive Fuels Handbook*; Society of Automotive Engineers: Warrendale, PA, 1990.
(2) *Standard Test Method for Distillation of Petroleum Products*, American Society for Testing and Materials: Philadelphia, *5.01*, 237–242.
(3) Greenfield, M.L.; Lavoie, G. A.; Smith, C. S.; Curtis, E. W. *SAE paper* **1998**, *982724*, 1–15.
(4) Smith, J. M.; Van Ness, H. C. *Introduction to Chemical Engineering Thermodynamics, 4th edition*, McGraw-Hill: New York, 1987.
(5) Prausnitz, J. M.; Lichtenthaler, R.; Azevedo, E. G. *Molecular Thermodynamics of Fluid-Phase Equilibria*, Prentice-Hall: Englewood Cliffs, NJ, 1986.
(6) Fredenslund, A; Jones, R. L., Prausnitz, J. M. *AIChE J.* **1975**, *21*, 1086.

MODELING OF A SMOLDERING CARBONACEOUS ROD

Ali Rostami[1], Jayathi Murthy[2] and Mohammad Hajaligol[1]

(1) Philip Morris USA, Research Center
P.O. Box 26583, Richmond, VA 23261

(2) Department of Mechanical Engineering,
Carnegie Mellon University, Pittsburgh, PA 15213

ABSTRACT

A transient 2-D model based on the first principles has been developed for the natural smoldering of a porous carbonaceous rod. Heat transfer is represented by the use of a two-temperature formulation whereby the solid and gas phases are considered to have separate and distinct temperatures interacting through an inter-phase heat exchange. The starting material first undergoes pyrolysis prior to oxidation of the remaining carbonaceous residue. The pyrolysis is assumed to consist of a set of reactions. Oxidation of the carbonaceous residue is accompanied by the formation of gas-phase combustion products, whose concentration is also computed. Calculations under unsteady conditions are done for a variety of smoldering cases with varying operating and boundary conditions. The model was validated by comparing the predictions with the experimental data on the smoldering burn rate and the maximum gas and solid temperatures. The computation captures the development of a steady combustion regime in which the burn front moves at a constant rate. More information can be obtained from the model including coal shape, gas and solid temperature profiles, product yields, solid density variations, and the effects of ignition conditions. The results are shown to be very sensitive to the availability of oxygen as well as heat losses.

INTRODUCTION

Smoldering of a porous carbonaceous rod is normally controlled by two main parameters: availability of oxygen to the combustion front and heat losses form it. The velocity of the combustion front into the carbonaceous fuel after the ignition by an external heat source and the peak temperature are two indicators of the sustenance of combustion. It is a transient process which is controlled by a combination of endothermic and exothermic chemical reactions in the pyrolysis and combustion zones, diffusion of oxygen to the combustion zone, diffusion of reaction products away from the sources, and heat transfer as well.

Since the early 1980's, several works on smoldering of cellulosic materials have been reported [1-7]. These works were focused on the generalization of combustion modeling in porous media. Both forward and reverse smoldering were considered, where a forced flow of air is resumed either in the direction of (forward) the smolder propagation or opposite to that (reverse). Analytical and numerical solutions were obtained for 1-D case of a semi-infinite packed fuel bed. In an attempt to model the steady state smoldering of a burning rod, Kinbara et al [8] used the a diffusion controlled approach to model the smoldering of a cylindrical fuel. The model was 1 D and the predicted behavior was in agreement with the measured burn rate. Ohlemiller [1] considered a burning cigarette as forward smoldering case, in which the air flow is in the same direction as the travelling combustion front. A comprehensive description of the mathematical formulation was presented by Ohlemiller [1], but no attempt was made to develop a solution technique for the multi-phase and multi-component system of equations.

We have recently embarked on an effort to develop comprehensive modeling software for the prediction of flow, heat transfer and chemical reaction in a burning porous rod. In this paper we present the natural smoldering combustion of the rod where no forced flow exists within the rod. A two-temperature formulation for the solid phase and the gas phase is then developed. In the subsequent sections, the model is described, followed by a description of the governing equations and the boundary conditions. Finally, the computed results are evaluated and recommendations are made.

MODEL DISCRIPTION

The modeling of pyrolysis and combustion in a smoldering fuel bed requires the solution of flow, heat and mass transfer through porous media. The gas and solid phases are treated separately. Pyrolysis occurs in the starting material through a set of pyrolysis reactions. The pyrolysis reactions result in the formation of a series of products. The pyrolysis products leave the solid phase, while the remaining carbonaceous residue is oxidized when exposed to high temperatures and oxygen. Some species in the gas phase may undergo further degradation reactions into other gas phase species, which is not considered in this study. In addition, we must also account for the evaporation of water, other volatile materials, and ash formation reactions as well.

The combustion process is initiated by applying a high temperature or a high heat flux at one end of the fuel rod for a fixed time. This initiates the pyrolysis reactions in a very narrow, nearly one-dimensional zone, followed by the oxidation of the carbonaceous residue. It is followed by combustion reactions in a larger two-dimensional cone, sustained by the diffusion of oxygen from the surrounding air through the porous fuel rod under smoldering conditions. The burn front moves axially, so does the combustion cone. For a given smoldering condition, the burn front is expected to travel at a constant velocity away from the lighted end of the rod.

Following the ignition, the instantaneous density of the starting material is calculated using a set of pyrolysis reactions and water evaporation represented by Arrhenius expression. The remaining solid residues react with oxygen at high temperatures which is assumed to follow Arrhenius relation as well. The kinetic parameters for the material of interest are obtained from literature.

The gas-phase transport equation is expressed as

$$\frac{\partial\ \rho(1-\phi)Y_i}{\partial t} + \nabla.(\rho \mathbf{V} Y_i) = \nabla \bullet (\rho D(1-\phi)\nabla Y_i) + R_i\phi \qquad (1)$$

where, ϕ is the porosity of the porous bed, ρ is the gas-phase mixture density, D is the diffusion coefficient of the species in the mixture and R_i is the volumetric rate of species production due to the oxidation reaction. All terms involving velocity V will be omitted for the case of smoldering.

The solid and gas phase energy equations are given as

$$(1-\phi)\rho_S C_{ps}\frac{\partial T_S}{\partial t} = \nabla\bullet\left(k_{s,eff}(1-\phi)\nabla T_S\right) + h_{S-g}\left(\frac{A}{V}\right)\left(T_g - T_S\right) + S_{solid} \qquad (2)$$

and

$$\frac{\partial}{\partial t}\left(\rho\ \phi h_g\right) + \nabla\bullet(\rho\vec{v}h_g) = \nabla\bullet(k_g\phi\nabla T_g) + h_{S-g}\left(\frac{A}{V}\right)\left(T_S - T_g\right) + S_{gas} \qquad (3)$$

respectively. For the solid phase equation, the source term S_{solid} would include the heat of reactions. $k_{s,eff}$ includes the radiation contribution to heat transfer in the solid by using Rosseland approximation to augment the solid conductivity. The interface heat exchange between the solid and gas phases is prescribed empirically by assuming a pore geometry. The correlation by Wakao and Kaguei [9] has been used in this study.

Boundary Conditions

For smoldering, the internal flow in the porous media is assumed to be negligible. The temperature for both the solid and gas phases at the inlet is held at T=1000 K until combustion starts; this typically takes 10-30 seconds depending on the conditions. After this, the temperature for both phases is set to T=300 K. All gas-phase species are assumed to have zero mass fraction at the inlet except oxygen, which assumed a mass fraction of 0.23 and nitrogen, which assumes a value of 0.77 throughout the smoldering process. At the outlet, a zero gradient condition is assumed for temperature and species mass fraction.

For smoldering, no flow boundary conditions are required. The gas and solid phase temperatures are subjected to a convective boundary condition at the lateral cylindrical boundary. All gas-phase species except oxygen are subjected to zero gradient conditions at the lateral boundary. For oxygen, different boundary conditions have been used for smoldering calculations, ranging from fully impermeable, to having a specified mass transfer coefficient.

Initially, both the gas and solid phase temperatures are set at 300 K throughout the domain. The mass fractions of oxygen and nitrogen are set at their environmental values of 0.23 and 0.77 respectively.

Details of the model as well as the numerical implementation appear in a manuscript submitted to *Journal of Applied Analytical Pyrolysis* and in another manuscript to be submitted to *Combustion and Flame*.

NUMERICAL IMPLEMENTATION

The geometry of the calculation domain is shown in Figure 1. A cylindrical axisymmetric fuel rod is assumed. A non-uniform structured mesh of 82x22 control volumes is used in the x and r directions respectively. The computational domain is set to be a porous zone in Fluent parlance.

The implementation of the models is done in a custom version of Fluent's structured mesh solver, Fluent 4.5. The domain is discretized into structured control volumes over which the conservation equations for mass, momentum, energy and chemical species are discretized.

A variable time step is used to do the calculations, with relatively large time steps of between 0.1-0.01 seconds during the initial passive heat-up stage followed by very smaller time steps once combustion commences. The size of the time step is controlled by the time scale of the oxidation reaction which is very fast.

RESULTS AND DISCUSSIONS

Numerous calculations were performed to identify the effects of the appropriate model parameters, numerical parameters and boundary conditions. A number of results including the effects of the surface heat transfer coefficient, overall mass transfer coefficient and the lighting conditions are reported here. The overall mass transfer coefficient, to which the results are very sensitive, depends on the convective coefficient on the surface as well as the diffusion coefficient in the porous wrapper if exists. In practice, the air velocity on the surface, hence the heat transfer and mass transfer coefficients, are highly unpredictable and vary significantly depending on the conditions of the air surrounding the rod. Therefore, an accurate comparison between the experimental results and the predictions was impossible, because most of the data available in the literature do not provide sufficient information on either the operating conditions or the physical properties.

Figure 2 shows the gas-phase temperature contours at steady state conditions for smoldering of a fuel rod made of cellulose. The steady state conditions prevail approximately 100 seconds after ignition. The kinetic parameters for this run were obtained from Kashiwagi and Numbu [10] and the thermophysical properties form Moussa et al. [11] and Dosanjh et al. [12]. The temperature at one end of the fuel rod was raised to 1000 K for 3 seconds. Combustion is initiated at this time and the temperature is set back to 300 K. The maximum temperature that normally occurs at the centerline (see Figure 1) strongly depends on the surface heat and mass transfer coefficients. The corresponding values for this run are 80 W/m^2K and 0.008 kg/m^2s respectively. The oxygen concentration for this case at the same time is shown in Figure 3. An oxygen-depleted region can be clearly seen in this figure.

The temperature of solid phase is slightly higher than the gas temperature (not shown in the figure). The difference is due to the fact that heat is generated in the solid phase as a result of chemical reactions and has to be transferred from the solid to the gas phase through the gas-solid interface. Therefore a solid-to-gas phase temperature gradient is required to keep the flow of heat, which is caused by the thermal resistance associated with the interface. The actual temperature difference between the two phases depends on the gas-solid interface resistance as well as the interface area, both of which are difficult to be accurately evaluated. The predicted temperature difference is generally between 1 and 2% of the gas temperature. For the case of Figures 2 and 3, the maximum solid temperature is generally 10 to 20 K higher than the maximum gas temperature depending on time and location.

The effects of peripheral heat losses are shown in Figure 4. For a given set of kinetic parameters, the fate of combustion is tied to the oxygen availability to as well as heat losses from the combustion zone. Having discussed the oxygen supply, we now turn to the heat transfer effects. The heat transfer mechanisms that are relevant to the combustion zone are axial and radial conduction and radiation in the porous rod as well as convection and thermal radiation form the surfaces. The first two are incorporated in the governing equations. An overall heat transfer coefficient is assigned to the lateral surface that includes the surface convection and radiation. The value of overall heat transfer coefficient, *h*, is varied from 20 to 100 W/m^{2}K. Fig. 5 shows the effects of the overall heat transfer coefficient on the steady state smoldering velocity and the gas maximum temperature respectively. The smoldering velocity reaches a high value of 16 mm/min for h=20 W/m^{2}K, while the maximum temperature reaches 1660 K for the same conditions. As h increases to 100 W/m^2 K, they drop to 5.3 mm/min and 850 K respectively.

CONCLUSIONS

Smoldering combustion of a cylindrical porous rod has been computed using Fluent 4.5. A variety of models have been incorporated for pyrolysis and oxidation as well as for heat transfer in porous media, including a two-temperature model for thermal non-equilibrium between gas and solid. Predictions of temperature and species concentration have been made. The results establish that the overall physics of the smoldering process is captured by the simulation, and the actual values of the gas and solid temperatures and the rate of burn are in reasonable agreement with the experimental data. The accuracy of the results depends strongly on a number of empirical parameters. The most significant parameters are the lateral mass transfer boundary condition for oxygen. The effects of these parameters are being studied and will be reported later. The numerics have proved to be stable and convergent and allow us to do computations with relative ease.
Though the effort has been successful in capturing the broad features of smoldering, as discussed above a number of improvements to the current model needs to be made.

REFERENCES

1. Ohlemiller, T. J., Modeling of Smoldering Combustion Propagation, *Prog. Energy Combust. Sci.*, Vol. 11, pp. 277-310, 1985.
2. Ohlemiller, T. J., and Lucca D. A., An Experimental Comparison of Forward and Reverse Smolder Propagation of Permeable Fuel Beds, *Combust. Flame* 54:131-147, 1983.
3. Leach, S. V., Rein, G., Ellzey, J. L., and Ezekoye, O. A., and Torero, J.L., Kinetics and Fuel Property Effects on Forward Smoldering Combustion, *Combust. Flame* 120: 346-358, 2000.
4. Torero, J. L., and Fernandez-Pello, A., Forward Smolder of Polyurethane Foam in a Forced Air Flow, *Combust. Flame* 106:89-109, 1996.
5. Buckmaster, J. and Lozinski, D., An Elementary Discussion of Forward Smoldering, *Combust. Flame* 104:300-310, 1996.
6. Ohlemiller, T. J., Bellan, J., and Rogers, F., A Model of Smoldering Combustion Applied to Flexible Polyurethane Foams, *Combust. Flame* 36:197-215, 1979.
7. Di Blasi, C, Modeling and Simulation of Combustion Processes, of Charring and Non-Charring Solid Fuels, *Prog. Energy Combust. Sci*., Vol. 19, pp. 71-104, 1993.
8. Kinbara, T., Endo, H. and Sega, S, Downward Propagation of Smoldering Combustion through Solid Materials, *11th Symp. Combust*., Pittsburgh, Pennsylvania, pp 525-531, 1967.
9. Wakao, N., and Kaguei S., "Heat and Mass Transfer in Packed Beds," Gordon and Breach, New York, 1982.
10. Kashiwagi T. and Nambu H., Global Kinetic Constants for Thermal Oxidative Degradation of Cellulosic Paper, Combustion and Flame, 88: 345-368, 1992.
11. Moussa, N. A., Toong, T. Y., and Garris, C. A., 16th Symposium on Combustion, The Combustion nstitute, Pittsburgh, p. 1447, 1976.
12. Dosanjh, S. S., Pagni, P. J., and Fernandez-pello, A. C, Forced Cocurrent Smoldering Combustion, Combustion and Flame, 68: 131-142, 1987.

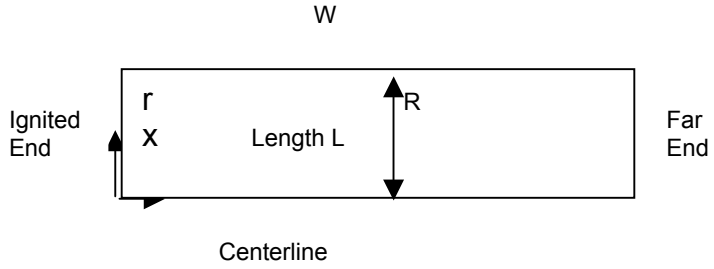

Figure 1 Geometry of Computational Domain

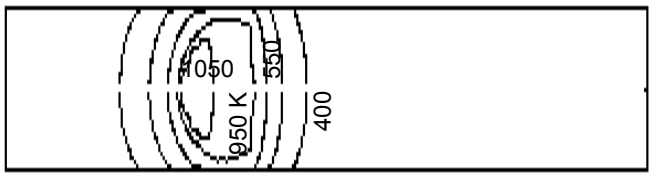

Figure 2. Gas Temperature Contours at 153 s after Initiation of smoldering

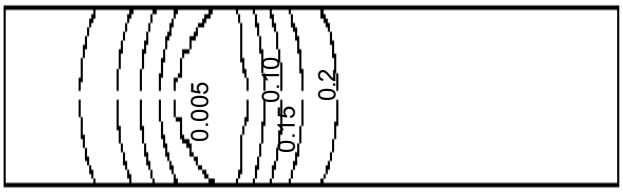

Figure 3. Oxygen Concentration Contours at 153 s after Initiation of Smoldering.

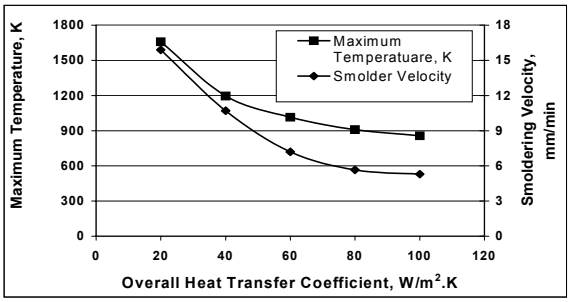

Figure 4. Effects of Heat Dissipation on Smoldering Velocity and Peak Temperature

A NOVEL APPROACH TO MOLECULAR MODELING OF TRANSPORT THROUGH INORGANIC NANOPOROUS MEMBRANES

M. A. Snyder[1], D. G. Vlachos[1], M. A. Katsoulakis[2]*

[1]Department of Chemical Engineering and Center for Catalytic Science and Technology (CCST), University of Delaware, Newark, DE 19716-3110

[2]Department of Mathematics and Statistics, University of Massachusetts, Amherst, MA 01003

Introduction

Numerous growth and permeation studies of nanoporous films have led to their attractiveness for application in separating gas mixtures with permselectivities approaching unprecedented subnanometer molecular resolution. The understanding and ability required for predicting macroscopic transport characteristics for diffusion of interacting molecular species through the complex lattices of these nanoporous inorganic membranes is key to the ultimate development of both traditional applications of this technology such as integrated reaction and separations devices, and more novel ones, such as substrates for growth of nanowires and chemical sensors.

Molecular simulations, specifically molecular dynamics and Monte Carlo algorithms, have emerged in the past few decades as preeminent computational tools for science and engineering research. Despite their widespread use and unprecedented insights into microscopic dynamics, such molecular simulations are computationally limited to short length and time scales, while inorganic membranes, such as zeolite films, invoke much larger scales (e.g., [1]) by way of macroscopic heterogeneities and imposed gradients.

On the opposite end of the modeling spectrum, continuum, Maxwell-Stefan models have been proposed in attempts to describe experimentally observed diffusion behavior. While these models have proven beneficial in fitting single and multi-component diffusion data, their phenomenological derivation does not capture the underlying microscopic diffusion dynamics and restricts their applicability to unrealistically simple diffusion lattices. Consequently, their accuracy as *a priori* predictive models is severely limited.

A major obstacle in addressing this multiscale modeling challenge is the lack of a rigorous mathematical and computational framework directly linking atomistic simulations and scales to complex mesoscopic and macroscopic phenomena dictated by microscopic intermolecular forces and material microstructure. A new mathematical framework has been introduced and validated through comparison with gradient Monte Carlo simulations, for modeling diffusion of interacting species in nanoporous materials over large length scales while retaining molecular scale information typically captured only by molecular simulations [2, 3].

Physical System and Microscopic Dynamics

Nanoporous membrane systems under imposed macroscopic gradients in concentration are the focus of this modeling work. In particular diffusion through inorganic membranes such as MFI and Faujasite zeolites is modeled. The mesoscopic framework is derived for systems characterized by intermolecular interactions between the adsorbed molecules (guests) and adsorbent (host) as well as between adsorbates (guest-guest interactions). Such diffusion systems are characterized by activation energies of duffusion that exceed the thermal energy of the system. As a result, diffusing molecules spend a significant amount of time at binding sites along the length of the pore, resulting in an activated hopping, or configurational diffusion mechanism. Fickian constitutive relations are rendered inadequate in this diffusion regime, the modeling of which is complicated by macroscopic gradients and material heterogeneities. An Arrhenius formalism is applied in this work to describe the microscopic diffusion dynamics of these systems. Such a mechanism[4] is characterized by an activation energy for diffusion depending only upon the energy of the departing site.

Validation of Mesoscopic Framework

Features of the mesoscopic framework. This new mathematical framework proposed to link microsopic properties to macroscopic diffusion phenomena, entails the use of newly developed mesoscopic equations derived rigorously from underlying master equations by coarse-graining statistical mechanics techniques in the case that diffusion occurs by a hopping mechanism. As a result of its fundamental derivation, the framework preserves microscopic dynamics. It has been shown mathematically that these equations are exact in the limit of long-range intermolecular interactions[2]. Furthermore, the coarse-grained continuum form of this framework results in the ultimate computational tractability for systems of realistic length and time scales through application of continuum numerical solution methods.

Steady state comparison to G-CTMC solutions. The validity of the mesoscopic model was first assessed in the microscopic limit for steady state behavior by comparing its solution to the corresponding solution obtained from Gradient-Continuous Time Monte Carlo (G-CTMC) simulations. Excellent agreement between the mesoscopic and MC steady state concentration profiles is depicted in **Figure1(a)** for longer-range potentials.

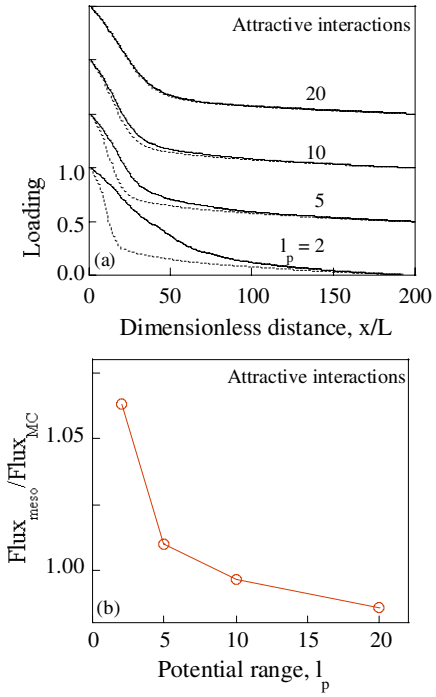

Figure 1. (a) Concentration profiles for Arrhenius dynamics obtained in 1D from MC (solid lines) and mesoscopic framework (dotted lines) using a piecewise constant interaction potential, with $\beta w = 4$ (attractive interaction strength) and different values of the interaction range, l_p. Note that the profiles have been shifted upward on the loading axis for the purpose of clarity. (b) Ratio of fluxes versus the potential range l_p.

Interestingly, the deviations seen in the predicted concentration profiles in **Figure 1(a)** for short-range potentials are not reflected in the predicted flux, **Figure 1(b)**. Similar validation of the mesoscopic solution was observed for systems with repulsive interactions, where the agreement between the G-CTMC and mesoscopic solutions is closer than the attractive case even for short potential lengths. It is important to note that all deviations between the mesoscopic and G-CTMC fluxes are smaller than those reported from one membrane to another in experiments, consequently suggesting the capability of mesoscopic models to accurately predict macroscopic permeation properties such as fluxes.

As seen in **Figure 1**, the concentration profiles for these systems, characterized by intermolecular interactions, are highly non-Fickian. That is, the profiles are highly non-linear. More dramatically, however, is the strong influence that interactions have upon the flux as depicted in **Figure 2**.

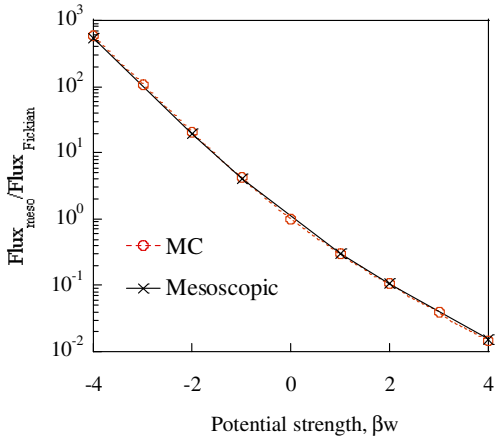

Figure 2. Steady-state fluxes versus potential strength in 1D for a piecewise constant potential with an interaction length of l_p=20.

As expected, repulsive interactions (negative *w*) greatly enhance the flux due to a reduction in activation energy of hopping, and attractive interactions (positive *w*) significantly inhibit diffusion due to an increase in the hopping activation energy caused by adsorbate-adsorbate interactions.

This drastic influence of intermolecular interactions upon the steady state flux further motivates development of the *fundamentally* derived mesoscopic framework to preserve the underlying microscopics while providing insight into macroscopic permeation properties at realistic length and time scales.

Extension of the Mesoscopic Framework

Multi-component diffusion. The extension of this mesoscopic framework to account for multi-component diffusion is shown in this work, focusing on mixtures of cyclohexane and benzene in faujasite through comparison to recently published multicomponent data[1]. Validation of the binary mesoscopic framework will be shown on the microscopic scale through comparison with multi-component G-CTMC simulation results.

Complex zeolite lattices. This rigorously derived mesoscopic framework allows for further extension of the mesoscopic models to account for complex zeolite lattice structures (e.g., MFI, Faujasite) defined by a variety of active sites available for diffusion, each uniquely contributing to the system energetics. We show here that the geometry and orientation of the pores of these three-dimensional materials strongly influence the ultimate membrane permeation characteristics and, consequently, begin to develop critical relations between microscopic properties and macroscopic diffusion phenomena within nanoporous membranes.

Acknowledgements

The work presented here has partially been supported by the National Science Foundation Career Award.

References

(1) Nikolakis, V.; Xomeritakis, G.; Abibi, A.; Dickson, M.; Tsapatsis, M.; Vlachos, D.G. *J. Membrane Sci.* **2000**, *84*, 209.

(2) Vlachos, D. G.; Katsoulakis, M. A. *Phys. Rev. Letters* **2001**, 85(18), 3898.

(3) Lam, R.; Basak, T.; Vlachos, D. G.; Katsoulakis, M. A. *J. Chem. Phys.* **2001**, 115(21), (*in press*).

(4) Metropolis, N.; Rosenbluth, A. W.; Rosenbluth, M. N.; Teller, A. H.; Teller, E.; *J. Chem. Phys.* **1953**, *21*, 1087.

O_2 dissociation on transition metals: Insights from first-principles calculations

Manos Mavrikakis and Ye Xu

Department of Chemical Engineering
University of Wisconsin - Madison,
Madison, WI 53706

Introduction

Dioxygen (O_2) dissociation on transition metal surfaces is of considerable research and practical interest both because many important industrial oxidation processes are heterogeneously *catalyzed* by transition metals and feature O_2 as the oxidizing agent and because O_2 dissociation is the first step toward the *corrosion* of various metals. Different mechanisms for O_2 dissociation have been identified on different metal surfaces. In the chemisorbed-precursor mechanism, the incident O_2 molecule initially chemisorbs intact [1]. Subsequent thermally driven kinetics determines selectivity between desorption and dissociation. On a number of transition metal surfaces, including Pt(111), Pd(111), Ni(111), Ag(110) and Cu(110), chemisorbed molecular oxygen species have been detected at temperatures below ~150 K. Two molecular states are frequently observed in vibrational spectroscopy: a peroxo form (O_2^{2-}), with an O-O stretching frequency of 610-650 cm^{-1}, and a superoxo (O_2^{-}) form, with a stretching frequency of 810-870 cm^{-1}. The precursors generally adopt the di-π orientation in which their molecular axes are parallel to the surface. Significant charge transfer from the substrate to the O_2 π_{2p}^* orbital weakens the O-O bond, which makes them likely precursors to O_2 dissociation. Because the existence of molecular O_2 precursors influences surface reaction kinetics, it is important to ascertain their characteristics and behavior. In this presentation, we will discuss our findings on O_2 dissociation on flat and stepped Cu and Au surfaces, but we will focus on our results on the O_2/Cu(111) system for the rest of this document.

The adsorption of atomic oxygen on Cu(111) has been studied extensively under a variety of experimental conditions. Threefold hollows are found to be the preferred adsorption sites for O atoms. The estimated saturation coverage of atomic oxygen ranges from 0.3 to 0.5 ML at room temperature. Extensive surface reconstruction is observed at medium to high oxygen coverage and at room temperature and above. There is no conclusive evidence for ordered overlayer structures until much higher temperature, probably with the onset of Cu_2O formation [2].

Molecularly adsorbed O_2 has also been detected on the Cu(111) surface. Several techniques, including UPS, XPS and HREELS, have revealed two chemisorbed molecular O_2 species, characterized by O-O stretching frequencies of 610 cm^{-1} and 820-870 cm^{-1} [3,4]. At low temperature a mixture of chemisorbed molecular oxygen and atomic oxygen species are found on the surface. The molecular species are not detected at temperatures above 170 K. The structural and electronic properties of these species are still not well understood, and the dissociation of O_2 on Cu(111) has not yet been studied theoretically.

We have performed periodic self-consistent DFT calculations to investigate the characteristics of various molecular and atomic oxygen configurations on Cu(111) and to explore the most likely pathways of O_2 dissociation. Because industrial heterogeneous catalysts consist of nanometer-sized metal particles supported on metal oxides that often induce strain on the surfaces of the metals [5], we have also examined the effect of strain on the thermochemistry and on the reaction barrier for O_2 dissociation on Cu(111) [6].

Methods

The calculations were performed using DACAPO [7]. Adsorption was allowed on only one of the two surfaces of a (2×2) unit cell used to construct the Cu(111) surface. The metal slab consists of four layers of Cu atoms. Successive slabs are separated by a vacuum equivalent to six layers of Cu. The Kohn-Sham one-electron valence states are expanded in a basis of plane waves with kinetic energies below 25 Ry. The exchange-correlation energy and potential are described by the generalized gradient approximation (GGA-PW91), and ionic cores are described by ultrasoft pseudopotentials. The surface Brillouin zone is sampled at 18 special *k* points. The calculated equilibrium PW91 lattice constant for bulk Cu is a = 3.66 Å, in good agreement with the experimental value of 3.62 Å.

Adsorption of atomic and molecular oxygen, and O_2 dissociation pathways are explored first on a fixed bulk-truncated surface at the equilibrium lattice constant. The effect of surface relaxation is investigated by relaxing the top two layers of the fixed surface. The fixed bulk-truncated surface is then compressed or stretched in the plane of the surface, whereon various properties are calculated again. The O-O bond length is chosen as the reaction coordinate in the determination of the dissociation pathway. The O-O stretching frequency is calculated using the harmonic oscillator approximation.

Results and Discussion

Atomic oxygen on Cu(111) The properties of adsorbed atomic oxygen are calculated at _ ML coverage. fcc sites are clearly preferred with a binding energy of -4.3 eV/O. For adsorption in an fcc or hcp site, the Cu atoms bound to the O atom relax outward by ~0.01 Å and move ~0.05 Å laterally away from the O atom to accommodate its presence. The energy barrier to diffusion is estimated to be ~0.45 eV on both the fixed and the relaxed surface. Increase in the surface work function suggests a net charge transfer to the O atoms, which makes these species ionic in character.

Molecular oxygen precursors on Cu(111) Calculations for molecular oxygen precursors are carried out with one O_2 molecule in every (2×2) unit

cell. Perpendicular O_2 precursors are calculated to be only marginally stable on Cu(111). The parallel (di-□) O_2 precursors are more strongly bound than the perpendicular precursors by ~0.5 eV/O_2 each. The di-□ precursors exist in several configurations on Cu(111). (For brevity, site names are abbreviated to their first letters. Thus, for instance, t-f-b stands for top-fcc-bridge). These include t-b-t, t-h(f)-b, and b-h(f)-b. Their binding energies are, respectively, -0.45, -0.52, and -0.56 eV/O_2 on a relaxed surface and are about 0.03 eV/O_2 less on a static surface. Charge transfer from the substrate quenches the magnetic moment of all but the t-b-t state, which still carries half (1.0 μ_B) of what a gas-phase O_2 molecule possesses. The O-O bond of the parallel precursors on Cu(111) is lengthened up to about 18% of the gas-phase O_2 bond length. Cu atoms not bound to the precursors sink between 0.05 to 0.14 Å in place. Those that are directly bound to the precursors do not show appreciable vertical displacement but move away from the precursors by ~0.05 Å horizontally. The O-O stretching frequencies of t-b-t, t-h-b and b-h-b states are found to be, respectively, 954, 789, and 729 cm^{-1}. The calculated frequencies are higher than experimental findings, but the two are in reasonable agreement given that GGA-PW91 calculations regularly over-predict vibrational frequencies by 5-10%. Based on their bond lengths and magnetic properties, the t-b-t precursor can be viewed as superoxo-like, and the t-h(f)-b and b-h(f)-b precursors can be viewed as peroxo-like.

O_2 dissociation on Cu(111) The most probable pathway starts with the most thermodynamically

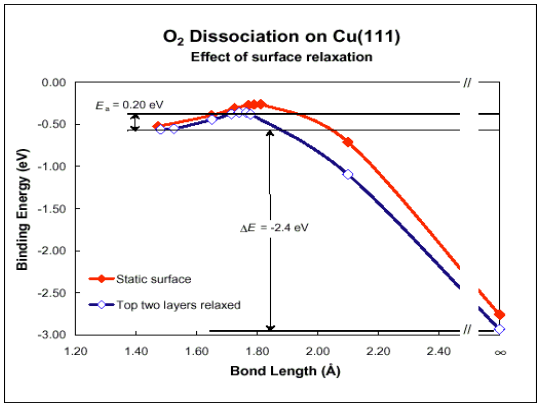

Figure 1. Reaction pathway for O_2 dissociation from b-h-b to fcc□2. The indicated activation energy and heat of reaction are those calculated on the relaxed surface.

,favorable precursor, b-h-b. The O-O bond would stretch until it breaks, upon which the two separated O atoms would fall into two adjacent fcc sites. The energy evolution along this pathway, both on the fixed and on the relaxed surface, is given in **Figure 1**. It can be seen that the transition state occurs early in the process, with a small activation energy barrier of 0.26 eV/O_2 above the initial b-h-b state on the fixed surface. On the relaxed surface the barrier is lowered to 0.20 eV/O_2. The overall O_2 dissociation process on Cu(111) is very exothermic, releasing 2.4 eV/O_2 of heat. Given the relative magnitudes of the precursor binding energy, activation energy and overall reaction exothermicity, O_2 precursor molecules will dissociate, rather than desorb, upon heating of the surface to yield chemisorbed O species. This agrees well with previous experimental findings [4]. The relaxed surface displays a high level of flexibility in the dissociation process, particularly after the transition state, indicating substantial involvement of surface Cu atoms in facilitating the breaking of the O-O bond.

Effect of strain We used a lattice constant of 3.50 Å (4.4% less than the equilibrium value of 3.66 Å) to model a compressed surface and 3.80 Å (3.8% more) to model a stretched surface. Lattice expansion leads to increased stability for all adsorbates. The binding energy of both atomic oxygen and molecular precursors are modified by ~∓0.1 eV by ~±4% strain. Roughly, for a 1% increase in the lattice constant, the binding energies of various adsorbates increase by ~0.03 eV. We also calculated the position of the *d*-band center of the Cu(111) surface as a function of strain. The results show a consistent up-shift of the *d*-band center with lattice expansion and thus increasingly strong surface-adsorbate interaction. This is in good agreement with the findings of previous theoretical studies on the effect of strain on the reactivity of several metal surfaces [8].

Figure 2 shows our results for the effect of strain

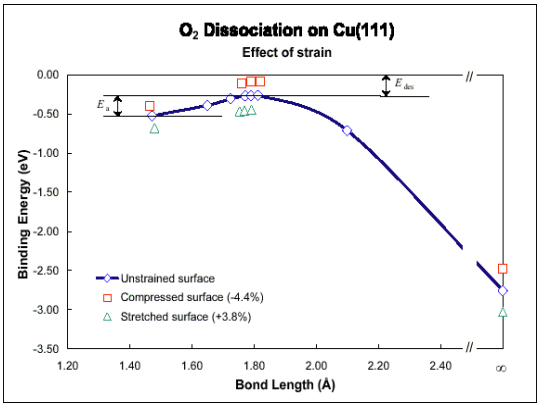

Figure 2. Effect of strain on O_2 dissociation from O_2 (b-h-b) to fcc□2 on a Cu(111) surface. Surface is not relaxed.

along the O_2 dissociation reaction path. Stretched surfaces stabilize the initial, transition, and final states. Because the transition state becomes significantly more stable in going from a = 3.66 to 3.80 Å, making the desorption barrier for the transition state correspondingly higher, the rate of O_2 dissociation can outperform the rate of O_2 desorption by 1-2 orders of magnitude depending on the temperature. Thus small supported Cu particles can show enhanced reactivity,

both because of strain and because of higher concentration of under-coordinated sites.

Acknowledgements

This research was supported in part by NSF cooperative agreement ACI-9619020 through computing resources provided by the National Partnership for Advanced Computational Infrastructure. Part of the calculations was performed on DOE supercomputing facilities (NERSC). YX gratefully acknowledges partial financial support from an NSF-GRT grant (Contract # EHR-9554586). MM thanks Shell Oil Company Foundation for a Faculty Career Initiation Award, which provided partial financial support.

References

(1) Nolan, P. D.; Wheeler, M. C.; Davis, J. E.; Mullins, C. B.; *Acc. Chem. Res.* **1998**, *31*, 798.
(2) Besenbacher, F.; Sprunger, P.T.; Ruan, L.; Olesen, L.; Stensgaard, I.; Lægsgaard, E. *Top. Catal.* **1994**, *1*, 325.
(3) Rajumon, M. K.; Prabhakaran, K.; Rao, C. N. R. *Surf. Sci.* **1990**, *233*, L237.
(4) Sueyoshi, T.; Sasaki, T.; Iwasawa, Y. *Surf. Sci.* **1996**, *365*, 310.
(5) Knop-Gericke, A.; Hävecker, M.; Schedel-Niedrig, T.; Schlögl, R. *Top. Catal.* **2000**, *10*, 187.
(6) Xu, Y.; Mavrikakis, M.; *Surf. Sci.* **2001**, *494*, 131.
(7) Hammer, B.; Hansen, L. B.; Nørskov, J. K. *Phys. Rev. B* **1999**, *59*, 7414.
(8) Mavrikakis, M.; Hammer, B.; Nørskov, J. K.; *Phys. Rev. Lett.* **1998**, *81*, 2819.

Physical properties of supported and unsupported transition metal nanoclusters

Shi-Ping Wang, Daniela S. Mainardi, and Perla B. Balbuena

Department of Chemical Engineering, University of South Carolina, Columbia, SC 29208

Introduction

Supported nanoclusters play a major role in many physical and chemical processes, such as those in heterogeneous catalysis and in the fabrication of nanostructured materials tailored to specific technological applications, e.g., micro and nanoelectronics, optoelectronics, and magnetic devices. Physical and electronic properties of metal nanoclusters deposited on various substrates have recently received a great deal of attention. [1] In particular, carbon-supported platinum particles are commonly used as catalytic materials in gas and liquid reactions. [2-4] Due to the high cost of platinum, many efforts are directed to optimizing its catalytic performance, which in turn requires a substantial understanding of the catalyst/substrate interactions,[5] and of the relationships between size, shape, and activity of the nanocatalysts [6,7] To minimize costs, alternative bi- and tri-metallic catalysts are proposed for several catalytic processes. In these cases, the mixing of the different elements on the surface of the nanoparticle gives rise to unexpected electronic and physical effects.

Computational methods

We use molecular dynamics (MD) simulations to compute the time evolution of a system consisting of a metal cluster of nanodimensions either in vacuum or deposited on a graphite substrate. The metal-metal interactions are treated within the Sutton-Chen potential model,[8] whereas the metal-graphite interactions are described by a Lennard-Jones potential. Details of the computational methods are given in a previous study. [9]

Heating and cooling curves are determined for each nanocluster and the melting temperature is obtained by the transition observed in the potential energy curve versus temperature. The melting/freezing characteristics are obtained for different cluster sizes and shapes.

Bimetallic systems are studied using a combination of Monte Carlo (MC) and MD methods. The MC technique is used to obtain the equilibrium atomic distribution on a bimetallic cluster of a given shape and size.[10,11] This equilibrium distribution is used as input to MD simulations where the dynamics of the system is investigated.

Results and Discussion

Figure 1 shows the variation of the potential energy for the 256-atom cube-shaped Pt cluster. In the heating process (squares), there is a clear energy jump in the temperature range from 1000 to 1100 K, this is due to the melting transition, note that the cluster melting temperature is much lower than that of bulk Pt metal (2041.15 K as determined experimentally). [12] The second set of data in Figure 1a corresponds to the cooling curve (circles), where the temperature is lowered starting from 1800 K down to 300 K. The system also shows a sharp liquid-solid transition, the freezing temperature, at T between 1000 and 900 K. The same time step was used for heating and cooling processes. Note that the portion of the curves corresponding to T > 1000 K are coincident for the cooling and heating processes, whereas for the portion below the melting temperature the potential energy is higher for the heating than for the cooling process. This indicates that the annealing process can easily find the lowest energy state for a given temperature, whereas during the heating process the system gets trapped in metastable states. Eventually, for simulation times sufficiently long, both curves should also agree at $T < T_{melting}$.

Similar phenomena have been observed in simulations of unsupported gold nanoclusters.[13] Another interesting behavior is observed also in the heating curve (Figure 2a), where the potential energy decreases from its value at 600 K to a lower value at 700 K and then increases again when T reaches 800 K. At 600 K, the cluster changes shape due to surface melting and surface atomic diffusion, adopting a semi-spherical shape. This change has also been observed in the experiment using high-resolution transmission electron microscopy, [14] and it is attributed to a structural solid-solid transition.

The melting behavior depends on the shape and size of the cluster. A spherical cluster constructed by carving the surface of a fcc cluster and deposited on the static surface of graphite is also studied. The potential energy for the 260-atom ball-shaped cluster is displayed in Figure 1b for the heating and cooling processes. Upon heating, the ball cluster also undergoes a solid-liquid jump in the temperature range from 1000 to 1100 K (squares), although the slope of the heating curve changes again at 1200 K. Practically no hysteresis is found between the heating and cooling curves at the liquid-solid transition for the ball-shaped cluster, as opposed to the case of the cubic cluster. This suggests that hysteresis loops may be more likely to be found in local minimum structures. The ball-shaped cluster also exhibits a behavior similar as that calculated for the cubic cluster at a temperature right below the melting transition, at T between 800 and 900 K, where the potential energy changes to a lower energy state presumably due to a solid-solid transition. [13] We suggest that the clusters undergo surface melting and surface atomic diffusion to form a lower energy structure before melting, as discussed in more detail below. Upon cooling, as in the case of the cubic cluster, the potential energy (circles) in the liquid range approaches values close to those of the heating process, whereas it reaches lower values in the solid region.

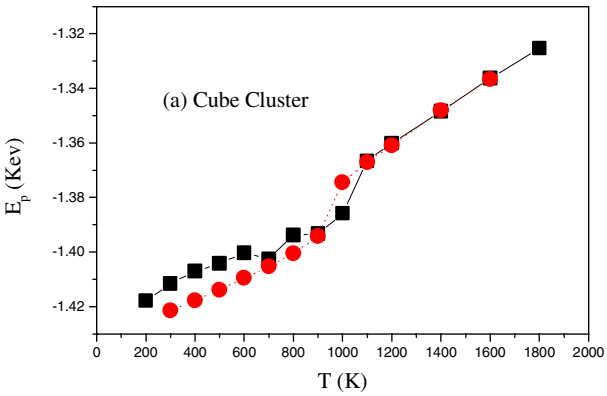

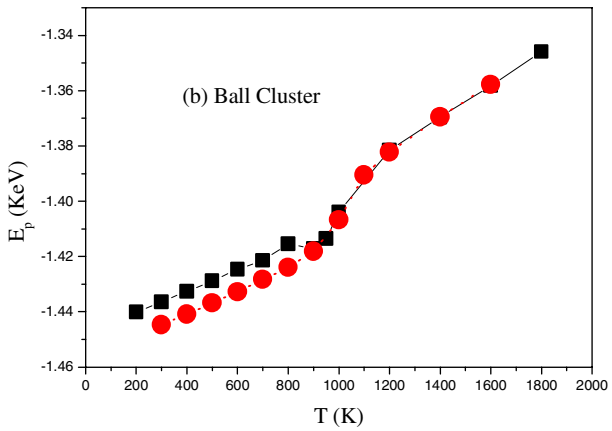

Figure 1. Calculated potential energy (E_p) variation, in KeV, for the heating (squares) and cooling (circles) curves. (a) Cube-shaped cluster. (b) Ball-shaped cluster.

Conclusions

The melting transition for a 256-atom Pt cluster of cubic shape deposited on a static graphite substrate is found in the range between 1000 and 1100 K, and the freezing temperature between 900 and 1000 K. At 600 K the cubic cluster starts experiencing a structural transformation, which is evidenced at 700 K by an increase in the interlayer separations from 1.83 to 2.13 Å, the outermost surface layers melt, and their atoms migrate to the layers closer to the substrate, a temperature-induced wetting phenomenon. At temperatures higher than 1000 K, melting takes place.

Results on bimetallic systems will be presented at the meeting.

Acknowledgement. This work is supported by the National Science Foundation (CTS-9876065), the Army Research Office (DAAD-19-00-1-0087), and the Department of Energy (DE-FG02-1ER15249)

References

(1) Jensen, P. *Rev. Mod. Phys.* **1999**, 1695-1735.
(2) Adzic, R. In *Electrocatalysis*; Lipkowski, J., Ross, P. N., Eds.; Wiley-VCH: New York, 1998, pp 197-242.
(3) Gunter, P. L.; Niemantsverdriet, J. W.; Ribiero, F. H.; Somorjai, G. A. *Catal. Rev. Sci. Eng.* **1997**, *39*, 77.
(4) Lambert, R. M.; Pacchioni, G., Eds. *Chemisorption and Reactivity on Supported Clusters and Thin Films: Towards an Understanding of Microscopic Processes in Catalysis*; Kluwer Academic Publishers: Dordrecht, 1997; Vol. 331.
(5) Zhu, J.; Somorjai, G. A. *Nano Letters* **2001**, *1*, 8-13.
(6) Joo, S. H.; Choi, S. J.; Oh, I.; Kwak, J.; Liu, Z.; Terasaki, O.; Ryoo, R. *Nature* **2001**, *412*, 169-172.
(7) Combe, N.; Jensen, P.; Pimpinelli, A. *Phys. Rev. Lett.* **2000**, *85*, 110-113.
(8) Sutton, A. P.; Chen, J. *Phil. Mag. Lett.* **1990**, *61*, 139-146.
(9) Huang, S.-P.; Balbuena, P. B. *Mol. Phys.* **2001**, in press.
(10) Mainardi, D. S.; Balbuena, P. B. *Langmuir* **2001**, *17*, 2047-2050.
(11) Mainardi, D. S.; Balbuena, P. B. *Int. J. Quant. Chem.* **2001**, in press.
(12) Benfield, R. E.; Filipponi, A.; Morgante, N.; Schmid, G. *J. of Organometallic Chemistry* **1999**, *573*, 299-304.
(13) Lewis, L. J.; Jensen, P.; Barrat, J. L. *Phys. Rev. B* **1997**, *56*, 2248-2257.
(14) Wang, Z. L.; Petroski, J. M.; Green, T. C.; El-Sayed, M. A. *J. Phys. Chem. B* **1998**, *102*, 6145-6150.

Thermochemistry and Kinetics for Alkyl + O2 Reactions in Hydrocarbon Oxidation.

Joseph W. Bozzelli, Chiung-Ju Chen, Chad Sheng
Dept of Chem Engrg, Chem and Envir. Sci.
New Jersey Institute of Technology, Newark, NJ 07102

Anthony M. Dean
Chemical Engineering Dept.,
Colorado School of Mines, Golden, CO 80401

ABSTRACT

Hydrocarbon radical reactions with oxygen are important in ignition and low temperature oxidation. Thermodynamic properties of reactants, products and transition states are determined by *ab initio* methods at the CBS-Q and G2 levels of theory based on the optimized geometry using B3LYP/6-31G(d,p) DFT and isodesmic reaction analysis. Rate coefficients for reactions of the energized adducts are obtained from canonical transition state theory. The reaction of an alkyl radical with O_2 typically forms an energized peroxy adduct with a calculated well depth of about 35 kcal/mole. This energized adduct can undergo isomerization, dissociate to new products or react back to reactants before stabilization. The stabilized adduct can also react through these same paths. Reactions of the adduct involve intramolecular hydrogen shifts, concerted HO2 molecular elimination, and subsequent reactions of the isomers formed include epoxide formation. Important product formation pathways involve pathways that are lower in energy than the initial reactants. The kinetics of the chemically-activated reaction between alkyl radicals and molecular oxygen are analyzed using quantum Rice-Ramsperger-Kassel (QRRK) theory for *k(E)* and a master equation analysis for collisional deactivation. Temperature and pressure dependent rate coefficients for the chemically-activated and the thermal reaction of the adducts and isomers are assembled into a mechanism and compared with experimental data for several systems. The predictions, using unadjusted rate coefficients, are consistent with literature observations over extended temperature and pressure ranges. Important new kinetic implications for chain branching and low-temperature ignition are discussed.

INTRODUCTION

Reactions of hydrocarbon radicals with molecular oxygen are important in atmospheric chemistry as well as in combustion processes. This type of elementary reaction is still under active investigation. The initially-formed energized peroxy radical has multiple reaction possibilities. The $C_2H_5 + O_2$ reaction represents an important model system to explore the kinetic consequences of these reactions; it contains many of the complexities of larger systems, yet is more amenable to detailed electronic structure calculations. An added advantage is that this reaction has been extensively studied experimentally. (Kaiser, 1995; Clifford et al., 2000, and references therein) There have also been several theoretical analyses of this system. Recent high-level *ab initio* calculations (Rienstra-Kiracofe et al., 2000) have characterized a new reaction pathway, concerted elimination to directly produce C_2H_4 and HO_2 from the initially-formed ethylperoxy adduct. This pathway was not considered in earlier kinetic analyses of the ethyl + O_2 system (Bozzelli et al., 1990; Wagner et al., 1990), but was included in a recent study. (Miller et al., 2000) One important aspect of this system is that most of the reaction channels of the energized adduct are higher in energy than the entrance channel and the concerted elimination channel is only a few kcal/mole lower. Thus, adduct stabilization is likely over an extended temperature range. Both Kaiser and Clifford et al. recognized the need to consider the kinetic consequences of subsequent thermal dissociation of this adduct in analyzing their experimental data. This reaction becomes increasingly important at higher temperatures, where the dissociation rate coefficient is larger.

METHODS

We used electronic structure theory to generate most of the input parameters needed to analyze this chemically-activated system. We wanted to assess whether this approach could accurately predict the temperature and pressure dependence of the various reaction channels. The potential energy surface was calculated at relatively high levels, and the rate coefficients for reactions of the energized adducts were obtained from canonical transition state theory (CTST). The rate coefficient for initial formation of ethylperoxy was calculated using variational transition state theory (VTST). We compared two models for collisional deactivation in conjunction with use of QRRK theory to estimate k(E). Finally, we incorporated the predictions for the individual branching fractions of the energized adducts and those for thermal dissociation of the stabilized adducts into a mechanism to illustrate where it is necessary to account for thermal dissociation. We conclude that this approach, with no adjustments to any of the parameters, permits a reasonably accurate description of this system. We also explore the kinetic implications of the direct formation of ethylene and HO_2 from CCOO•.

TABLE 1. Isodesmic Working Reactions

Isodesmic Reaction	ΔH^f_{298}	Method
CH_3CH_2OOH + CH_3OH = CH_3CH_2OH + CH_3OOH	-39.89	CBS-Q
CH_3CH_2OOH + CH_3OH = CH_3CH_2OH + CH_3OOH	-40.06	G2
CH_3CH_2OOH + CH_3OH = CH_3CH_2OH + CH_3OOH	-39.96	G2//B3
$CH_3CH_2OO•$ + CH_3OOH = $CH_3OO•$ + CH_3CH_2OOH	-6.72	CBS-Q
$CH_3CH_2OO•$ + CH_3OOH = $CH_3OO•$ + CH_3CH_2OOH	-6.77	G2
$•CH_2CH_2OOH$ + CH_3OH = CH_3CH_2OOH + $C•H_2OH$	10.92	CBS-Q
$•CH_2CH_2OOH$ + CH_3OH = CH_3CH_2OOH + $C•H_2OH$	10.49	G2
(Specie Calculated Are In Bold.)	**kcal/mol**	

DISCUSSION OF RESULTS

The calculated apparent rate coefficients for direct formation of the major product channels of chemically-activated CCOO•, including both the master equation and modified strong collision results, are shown in Fig. 2 for P = 1 atm N_2. Both models give remarkably similar predictions. In this case, the barriers for the major channels are reasonably close in energy, and this would be expected to minimize the differences between the two deactivation models. The dominant reaction up to almost 1000K is formation of the ethylperoxy adduct, while the direct formation of ethylene and HO_2 from the energized adduct dominates above 1000 K. The production of ethylene and HO_2 via the sequential pathway is much less important, due to the higher barrier for isomerization.

At 750K, the ethylene channel decreases with pressure, as expected, but the overall predicted pressure effect is quite small. Stabilization becomes the dominant channel at higher pressures. The

production of the hydroperoxyethyl isomer is much less likely than ethylperoxy, reflecting the lower energy pathway from ethylperoxy directly to ethylene, which bypasses hydroperoxyethyl. Significant differences between the collisional deactivation models only appear at very low pressures, with the master equation model showing less stabilization. The smaller number of collisions at lower pressures enhances the energy-dependent reaction channels. Since the master equation model allows multiple deactivation steps prior to "complete" deactivation, this increases the probability for reaction with this model and thus decreases the stabilization rate coefficient.

Table 2 QRRK Input Parameters

Reaction	A	n	Ea
$C_2H_5 + O_2 = C_2H_5OO•$	$8.82x10^9$	1.12	0.0
$C_2H_5OO• = C_2H_5 + O_2$	$2.46x10^{18}$	-1.07	35.32
$C_2H_5OO• = H_2C•CH_2OOH$	$7.90x10^6$	1.79	35.82
$H_2C•CH_2OOH = C_2H_5OO•$	$5.89x10^6$	1.04	18.01
$C_2H_5OO• = CH_3CHO + OH$	$1.32x10^9$	1.37	41.59
$C_2H_5OO• = C_2H_4 + HO_2$	$8.80x10^5$	2.24	29.61
$C_2H_5OO• = CH_3CH_2O• + O•$	$2.98x10^{15}$	-0.09	61.6
$H_2C•CH_2OOH = C_2H_4 + HO_2$	$6.44x10^{10}$	0.52	16.18
$H_2C•CH_2OOH = H_2COCH_2 + OH$	$6.62x10^9$	0.72	15.41

$C_2H_5OO•$ ν_1=373 cm^{-1} (degen=4.13) ν_2 = 1256 cm^{-1} (10.53) ν_3 = 3053 cm^{-1} (5.34)

$H_2C•CH_2OOH$: ν_1=289 cm^{-1} (degen=6.10) ν_2 = 1161 cm^{-1} (8.16) ν_3 = 3179 cm^{-1} (5.23)

σ = 4.94 Å ε/k = 450.

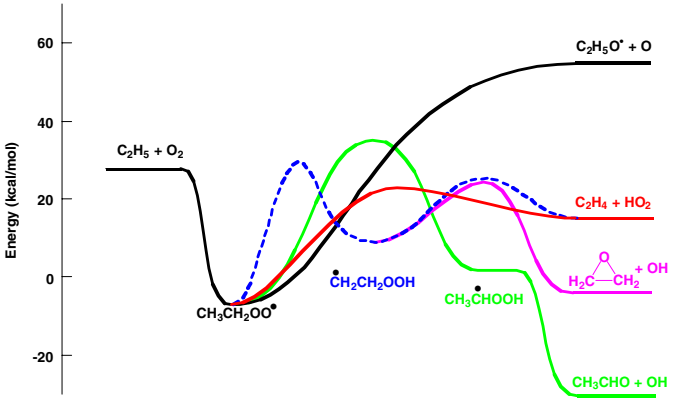

Fig. 1 Potential energy diagram for the C_2H_5 +O_2 reaction. There are the two pathways to C_2H_4 + HO_2. The red line represents the direct elimination, while the blue dashed line represents a sequential pathway–first isomerization to hydroperoxyethyl, which is followed by β-scission

Fig. 3 compares the predictions of the ethylene yield as a function of pressure at 298K to that measured by Kaiser. The sharp decrease with pressure, due to increased stabilization of the energized adduct prior to the concerted elimination, is well predicted with both collisional deactivation models. The predictions indicate that virtually all of the ethylene is produced via the direct elimination channel, as opposed to that produced via isomerization to hydroperoxyethyl followed by β-scission.

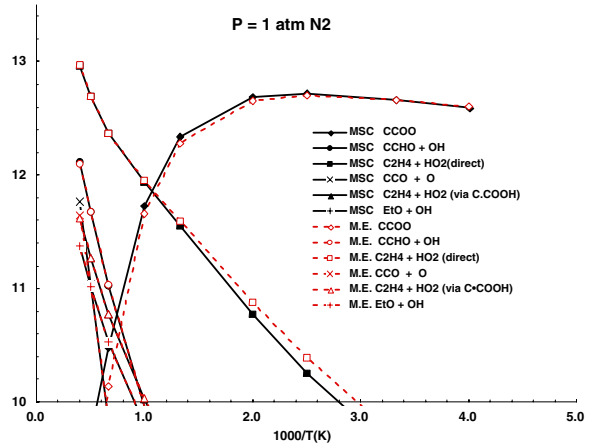

Fig. 2 The predicted effect of temperature upon the apparent rate coefficients for the major channels of the chemically-activated reaction C_2H_5+O_2, using both the modified strong collision model and a master equation model for collisional deactivation.

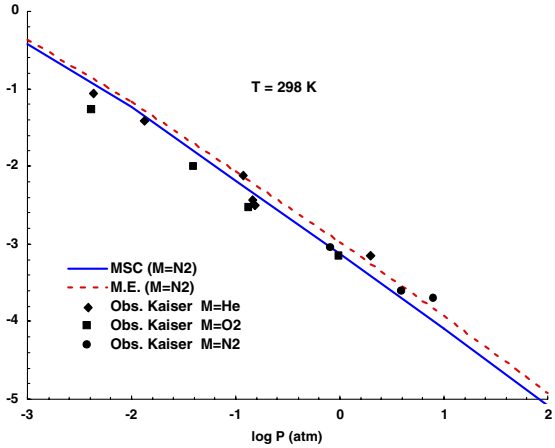

Fig 3. Comparison of Ethylene Yield at 298K between Kaiser's experimental data with model predictions.

At this low temperature, it is possible to compute to ethylene yield directly by taking the ratio of the sum of the predicted rate coefficients for "direct", i.e., chemically-activated, ethylene production to the total predicted "direct" rate coefficient. The temperature is sufficiently low that any contribution from dissociation of the stabilized adduct is insignificant. However, as the temperature is increased and the thermal dissociation rate coefficient increases, it is necessary to generate a small mechanism to allow comparison to the data. The reactions considered includes all the "direct" reactions, as well as further reactions of the stabilized adducts formed in the direct reactions. Also included are the other reactions used by Kaiser to model his data. Since the QRRK rate coefficients are dependent on both temperature and pressure, we needed to use different sets of coefficients for each set of experimental conditions with different T and P. (This is a good example of the utility of using Chebyshev fits (Venkatesh et al., 1997) to capture k(T,P) so that one set of rate coefficients could be used for all conditions.)

The importance of the subsequent reactions of the stabilized adducts can be seen in Fig. 4, where predictions of the temperature dependence of the ethylene yield are compared to Kaiser's data. At

253 K and 373 K, the ethylene yield computed by only considering the direct channels is identical to that obtained by numerical integration of the complete mechanism. However, at 513K, the direct yield is significantly smaller than that obtained by the mechanism. Here the temperature is sufficiently high that thermal dissociation of ethylperoxy contributes substantially to the overall ethylene yield. Predictions based on the overall mechanism are in good agreement with Kaiser's observations.

In addition to capturing the temperature and pressure dependence of the ethylene yield, the predicted rate coefficient for overall ethyl decay is also in reasonable agreement with Kaiser's data. There is little difference in the "direct" QRRK result and that obtained via numerical integration. For the integration, we used Kaiser's method (comparing the computed consumption of ethane to the formation of ethyl chloride) to obtain k_{tot}. This approach lead to slightly different values at different times, and the results were averaged. The agreement with Kaiser's data is encouraging. The increase in predicted rate coefficient at the lower temperatures reflects the temperature dependence of adduct formation rate, while the decrease seen in most cases at 460K reflects the onset of falloff. Here the apparent rate coefficient decreases as the adduct begins to react back to reactants.

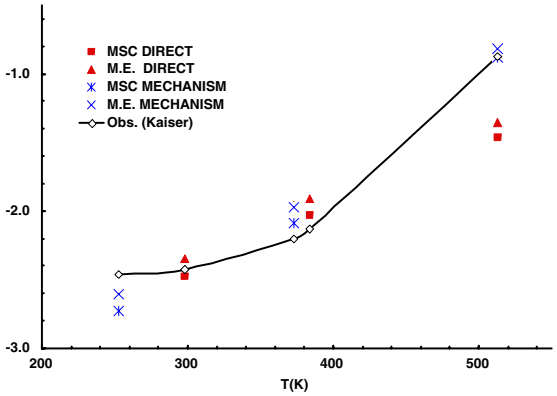

Fig. 4 Comparison of predicted effect of temperature on the ethylene yield to the observations of Kaiser. Points labeled "DIRECT" are obtained by taking the ratio of the chemically-activated rate coefficients for production of ethylene to the total apparent chemically-activated rate coefficient. Points labeled "MECHANISM" were calculated from the results of numerically integrating the systems of reactions.

We have also used our approach to compare predicted HO_2 yields to those measured in the recent measurements of Clifford et al. (2000). Those experiments were done over a wider temperature range at lower pressures and lower radical concentrations than Kaiser's. The temporal evolution of HO_2 was measured. Biexponential time behavior for HO_2 formation was observed and attributed to the reactions of the stabilized peroxy adduct. These researchers were able to extract both a total and a prompt HO_2 yield. The prompt yield should correspond to that obtained from the QRRK chemical-activation analysis, while the total yield corresponds to that obtained using the mechanism, which accounts for these reactions as well as the reactions of the stabilized adduct. Clifford et al. obtained the HO_2 yield by comparing the HO_2 signal obtained with ethane to that obtained with methanol, where the yield is expected to be unity. This was necessitated by the importance of HO_2 recombination under the experimental conditions. We obtained our predicted yields in an analogous manner. We found that the yields were not always constant with time, especially at lower temperatures, and the values reported represent an average over the time scale of the Clifford et al. experiments. We used both collisional deactivation models for our comparisons.

Fig. 5 compares the predicted total HO_2 yield as a function of temperature to that measured by Clifford et al. Again we obtain similar results with both the modified strong collision assumption and the master equation, and both sets of predictions agree nicely with the observations of Clifford et al. Particularly encouraging was the correct prediction of the observed rapid increase above 500K. It is essential to include the dissociation of the ethylperoxy adduct at 650K, as can be seen by the comparison of the results for direct HO_2 production to those obtained using the mechanism. Only approximately one-third of the overall HO_2 yield can be seen to come directly from the energized adduct. On the other hand, at 500K virtually all of the yield can be attributed to the direct reaction. At this lower temperature, the contribution from dissociation of the stabilized adduct is negligible.

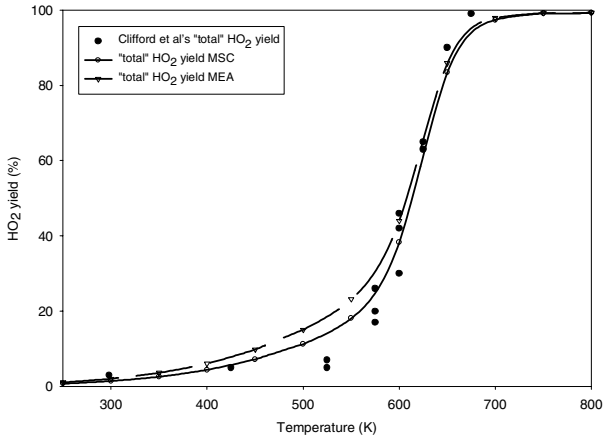

Fig. 5 Comparison of predicted total yield of HO_2 to that observed by Clifford et al.

IMPLICATIONS FOR LOW TEMPERATURE IGNITION

The conventional approach to describe low-temperature ignition kinetics, especially the region of negative temperature coefficient, considers the following reactions (Walker et al., 1997):

$$R^{\bullet} + O_2 \rightleftharpoons ROO^{\bullet} \quad (1)$$

$$ROO^{\bullet} + RH \longrightarrow ROOH + R^{\bullet} \quad (2)$$

$$ROOH \longrightarrow RO^{\bullet} + HO^{\bullet} \quad (3)$$

$$ROO^{\bullet} \longrightarrow R^{\bullet}OOH \quad (4)$$

$$R^{\bullet}OOH \longrightarrow RO + HO^{\bullet} \quad (5)$$

$$R^{\bullet}OOH + O_2 \longrightarrow \text{branching} \quad (6)$$

($R^{\bullet}$ is an alkyl radical, $RO^{\bullet}$ is an alkoxy radical and RO is generally a cyclic ether. $R^{\bullet}OOH$ is often written as QOOH, but we use the $R^{\bullet}OOH$ notation to emphasize the free radical character of this species.) If the temperature is sufficiently low that the equilibrium in (1) is shifted to the right, the subsequent reactions of RO_2 can lead to the chain-branching (Rxns. 3 and 6) needed for ignition. However, as

the temperature rises, the equilibrium in (1) shifts to the left, reducing the RO_2 concentration and thus slowing down the overall rate, i.e., producing a negative temperature coefficient of reaction rate. Particularly noteworthy in this mechanism is the importance of the isomerization reaction (Rxn. 4); without this, chain branching via Rxn. (6) cannot occur. In ethane oxidation, the *newly-identified* direct pathway for production of ethylene and HO_2 from ethylperoxy is much faster than Rxn. 4. This competing fast reaction necessarily reduces the amount of R˙OOH that can be produced via Rxn. 4. Here the amount of chain branching via Rxn. 6 will be substantially reduced. Although more complex fuels might well have lower barriers to isomerization [by having the internal hydrogen transfer via a less strained ring (6- vs. 5-member) or by abstracting secondary or tertiary hydrogens rather than the primary hydrogens in ethyl], the possibility of concerted elimination of HO_2 from RO_2 in these fuels will generally result in formation of less R˙OOH, thus reducing the overall branching rates. Thus there is a need to revisit these systems to see if new branching pathways are needed to accurately describe low-temperature ignition.

REFERENCES

(1) Bozzelli, J. W.; Dean, A. M. *J. Phys. Chem.* **1990**, *94*, 3313-3317.
(2) Clifford, E. P.; Farrell, J. T.; DeSain, J. D.; Taatjes, C. A. *J. Phys. Chem A* **2000**, *104*, 11549-11560.
(3) Kaiser, E. W. *J. Phys. Chem.* **1995**, *99*, 707-711.
(4) Miller, J. A.; Klippenstein, S. J.; Robertson, S. H. "A Theoretical Analysis of the Reaction Between Ethyl and Molecular Oxygen"; 28th International Symposium on Combustion, 2000, Edinburgh, Scotland.
(5) Rienstra-Kiracofe, J. C.; Allen, W. D.; Schaefer III, H. F. *J. Phys. Chem. A* **2000**, *104*, 9823-9840.
(6) Venkatesh, P. K.; Dean, A. M.; Cohen, M. H.; Carr, R. W. *Reviews in Chemical Engineering* **1997**, *13*.
(7) Wagner, A. F.; Slagle, I. R.; Sarzynski, D.; Gutman, D. *J. Phys. Chem.* **1990**, *94*, 1853-1868.
(8) Walker, R. W.; Morley, C. Basic Chemistry of Combustion. In *Low-Temperature Combustion and Autoignition*; Pilling, M. J., Ed.; Elsevier: Amsterdam; New York, 1997; pp 1-124.